

Complete dynamical analysis of a neuron model

Andrey Shilnikov

Received: 4 April 2011 / Accepted: 5 April 2011 / Published online: 29 April 2011
© Springer Science+Business Media B.V. 2011

Abstract In-depth understanding of the generic mechanisms of transitions between distinct patterns of the activity in realistic models of individual neurons presents a fundamental challenge for the theory of applied dynamical systems. The knowledge about likely mechanisms would give valuable insights and predictions for determining basic principles of the functioning of neurons both isolated and networked. We demonstrate a computational suite of the developed tools based on the qualitative theory of differential equations that is specifically tailored for slow–fast neuron models. The toolkit includes the parameter continuation technique for localizing slow-motion manifolds in a model without need of dissection, the averaging technique for localizing periodic orbits and determining their stability and bifurcations, as well as a reduction apparatus for deriving a family of Poincaré return mappings for a voltage interval. Such return mappings allow for detailed examinations of not only stable fixed points but also unstable limit solutions of the system, including periodic, homoclinic and heteroclinic orbits. Using interval mappings we can compute various quantitative characteristics such as topological entropy and kneading invariants for examinations of global bifurcations in the neuron model.

Keywords Neuron model · Bifurcation · Bursting · Bistability · Poincaré mapping · Parameter continuation · Complex dynamics

1 Introduction

Individual neurons can generate various complex oscillations known as bursting, formed by alternating fast repetitive spiking and quiescent or subthreshold oscillatory phases. Bursting is a manifestation of composite, multiple timescale dynamics observed in various fields of science as diverse as food chain ecosystems, nonlinear optics, medical studies of the human immune system, and neuroscience. In neuroscience, bursting is observed, but not limited to, in pathological brain states [1, 2], particularly, during epileptic seizures [3, 4].

A single neuron can demonstrate various bursting patterns endogenously, varying in response to external disturbances due to synapses or to intrinsic factors such as channel noise. The coexistence of bursting and tonic spiking, as well as several different bursting modes, has been observed in models [5–9] and experimental studies [10–12]. The role of bursting is especially important for rhythmic movements determined by Central Pattern Generators (CPGs) [13]. CPGs are small polymorphic neural circuits controlling various vital repetitive locomotive functions [14] such as cardiac beating, respiration and walking of humans, swimming and crawling of leeches, etc. [15].

A. Shilnikov (✉)
Neuroscience Institute, Department of Mathematics
and Statistics, Georgia State University, Atlanta,
GA 30303, USA
e-mail: ashilnikov@gsu.edu

Currently, of very special interest are the bursting polyrhythmic dynamics in a multifunctional CPG [16] in which each oscillatory attractor corresponds to a specific rhythm on a specific timescale associated with a particular type of the rhythmic behavior of an animal. Such a CPG can drive multiple behaviors and switch between different neuronal rhythms upon various conditions [17, 18]. The multistability enhances the complexity and flexibility of the nervous and locomotive systems [19]. Examples include the Tritonia swimming types, switching between trot and gallop in some animals, and switching between crawling and swimming in leeches.

Deterministic description of endogenous oscillatory activities, such as tonic spiking and bursting, in neuronal dynamics is based on the examination of generic properties of various mathematical and realistic models derived through the Hodgkin–Huxley formalism. A typical neuronal model falls into a special class of dynamical systems with at least two distinct timescales, i.e. slow–fast systems. Geometric configurations of neuron models for bursting, pioneered by Rinzel [20], were further developed by Ermentrout [22], Bertram et al. [6], Guckenheimer [23] and by Izhikevich [24, 25]. Dynamics of such models are determined by and centered around the attracting sections of the slow-motion manifolds, which are composed of equilibria and limit cycles of the fast subsystem [26–32]. These manifolds constitute the backbones of bursting patterns in a neuronal model. A typical Hodgkin–Huxley model possesses a pair of such manifolds [20]: quiescent and tonic spiking. The existing classifications of bursting are based on codimension-one bifurcations that initiate or terminate the fast trajectory transitions between slow-motion manifolds in the 3D phase space of a model. These classifications single out the classes of bursting by subdividing neuronal models into the following types: elliptic or Hopf-fold; square-wave burster, or fold-homoclinic; parabolic, or circle-circle class describing top-hat models.

The slow–fast dissection has been proven to work very well for most low-order models of bursting neurons *as long as* they stay far from the transitions from and to bursting. However, it provides less insight into the bifurcations of bursting which are often due to reciprocal interactions involving both slow and fast dynamics and leading to the emergence of novel dynamical phenomena that can *only* occur in the entire sys-

tem, not in any of its subsystems. Moreover, near transitions, the bursting behavior becomes rather complex, and may often exhibit deterministic chaos [33–41].

Analysis of bursting transformations requires the use of nonlocal bifurcation tools, including Poincaré return mappings [42–44]. Mappings have been actively employed in computational neuroscience, see [38, 45–49] and references therein. A drawback of mappings constructed from time series is their sparseness as they reflect only dominating attractors of a system. A new, computer-assisted method for constructing a complete family of *onto* mappings for membrane potentials of Hodgkin–Huxley neuronal models was proposed in [41, 50, 51] following [52]. Using this approach we have studied complex bursting bifurcations in a leech heart interneuron model and revealed that the cause of complexity is homoclinic tangles of saddle periodic orbits [49].

One goal of this paper is to give a comprehensive description of bifurcations leading to the emergence of complex, coexisting bursting patterns in a reduced model of the leech heart interneuron. The number of open problems in mathematical neuroscience, including global bifurcations in models and networks, remains quite large [23]. The range of bifurcations and dynamical phenomena giving rise to bursting *transcends* the existing classification schemes. The list of bifurcations occurring on the edge of bursting includes various homoclinic inclination/orbit-flip bifurcations of saddle, the blue sky catastrophe, bistability of bursting with tonic spiking, and subthreshold oscillations like MMOs, torus-canard formation and breakdown, etc. [38, 41, 46, 53–60]. Such bifurcations are frequently observed in many neuronal models and cannot be explained by the slow–fast dissection method. For the past decade there was a single mechanism rigorously examined [33] for square-wave burster: its key feature is—chaotic dynamics of finite subshift type. The recent breakthrough in this direction came with two novel generic mechanisms—both related to homoclinic bifurcations of saddle-node periodic orbits. The first mechanism, based on the blue sky catastrophe [42–44, 58, 61], describes a reversible and continuous transition between tonic spiking and bursting. The feature of the other transition mechanism, due to non-central homoclinics [62] to a saddle-node orbit, is bistability of a neuron such that it can fire tonic spikes or exhibit bursting, depending on its initial state. Moreover, bistable neurons at the edge of the

transition show transient chaos with an unpredictable number of burst trains followed by regular tonic spiking. This phenomenon is a direct consequence of the Smale horseshoe dynamics in the system [63]. Neither transition can be explained in terms of slow-fast dissections. Further systematic development of dynamical neuroscience calls for new bifurcation methods tailored specifically to multiscale neuronal models.

2 Reduced leech heart interneuron model

Several reduced models of a leech heart interneuron [5] were introduced in Ref. [64]. The “least” complex model is given by the following three equations [39, 50, 58, 64] derived through the Hodgkin–Huxley gated variables formalism [65]:

$$\begin{aligned}
 C \frac{dV}{dt} &= -I_{Na} - I_{K2} + I_L - I_{app} - I_{syn}, \\
 I_L &= \bar{g}_L (V - E_L), I_{K2} = \bar{g}_{K2} m_{K2}^2 (V - E_K), \\
 I_{Na} &= \bar{g}_{Na} m_{Na}^3 h_{Na} (V - E_{Na}), m_{Na} = m_{Na}^\infty(V), \\
 \tau_{Na} \frac{dh_{Na}}{dt} &= h_{Na}^\infty(V) - h, \\
 \tau_{K2} \frac{dm_{K2}}{dt} &= m_{K2}^\infty(V) - m_{K2}, \tag{1}
 \end{aligned}$$

where $C = 0.5$ nF is the membrane capacitance; V is the membrane potential; I_{Na} is the fast voltage gated sodium current with slow inactivation h_{Na} and fast activation m_{Na} ; I_{K2} is the persistent potassium current with activation m_{K2} ; I_L is leak current and I_{app} is a constant polarization or external applied current. The maximal conductances are $\bar{g}_{K2} = 30$ nS, $\bar{g}_{Na} = 200$ nS and $g_L = 8$ nS, and the reversal potentials are $E_{Na} = 0.045$ V, $E_K = -0.070$ V and $E_L = -0.046$ V. The time constants of gating variables are $\tau_{K2} = 0.25$ s and $\tau_{Na} = 0.0405$ s. We would like to point out that the time constant of the activation of the potassium current is lowered to the value $\tau_{K2} = 0.9$ and the applied current is no longer zero: $I_{app} = 0.006$ nA whenever we will discuss the occurrence of the blue sky catastrophe in the model (Fig. 5).

The steady-state values of gating variables, $h_{Na}^\infty(V)$, $m_{Na}^\infty(V)$, $m_{K2}^\infty(V)$, are given by the following Boltz-

mann equations:

$$\begin{aligned}
 h_{Na}^\infty(V) &= [1 + \exp(500(0.0333 - V))]^{-1}, \\
 m_{Na}^\infty(V) &= [1 + \exp(-150(0.0305 - V))]^{-1}, \tag{2} \\
 m_{K2}^\infty(V) &= [1 + \exp(-83(0.018 - V + V_{K2}^{shift}))]^{-1}.
 \end{aligned}$$

The quantity V_{K2}^{shift} has become a genuine bifurcation parameter for this model: it is the deviation from experimentally averaged voltage value $V_{1/2} = 0.018$ V corresponding to semi-activated potassium channel, i.e. $m_{K2}^\infty(0.018) = 1/2$. Variations of V_{K2}^{shift} move the slow nullcline $\frac{dm_{K2}}{dt} = 0$ in the V -direction in the 3D phase. This delays/speeds the activation of m_{K2} when the parameter is moved toward negative/positive, respectively values. Dynamically, this results in the neuron firing tonically, or becoming hyperpolarizingly quiescent, respectively. The range of V_{K2}^{shift} is $[-0.025, 0.0018]$ V in this study. The upper boundary of the interval corresponds to the hyperpolarized quiescent state of the neuron, whereas it fires tonically at lower V_{K2}^{shift} values. As the parameter is varied within this interval, the model undergoes multiple transformations in the bursting activity. We must note here that responses of dynamics of the model to changes of V_{K2}^{shift} are not totally equivalent to variations of an applied (or I_{pol}) current, as the latter affects the topology of the slow-motion manifolds of the fast (v, h_{Na}) subsystem, which remains intact while V_{K2}^{shift} is varied.

3 Slow-fast paradigm

To move forward on the analysis of the model, we introduce some basics of the theory of slow-fast systems.

Consider a slow-fast system

$$\begin{aligned}
 \varepsilon \dot{\mathbf{v}} &= F(\mathbf{v}, m), \\
 \dot{m} &= G(\mathbf{v}, m, \alpha), \tag{3}
 \end{aligned}$$

where $\mathbf{v} \in R^n$, $n \geq 2$, $m \in R^1$ for simplicity, $|\varepsilon| \ll 1$ is a small parameter, α is a single bifurcation parameter, and functions F, G are smooth. Rescaling the time $t = \varepsilon \tau$ changes (3) to the form

$$\begin{aligned}
 \mathbf{v}' &= F(\mathbf{v}, m), \\
 m' &= \varepsilon G(\mathbf{v}, m, \alpha), \tag{4}
 \end{aligned}$$

in new time τ . In the singular limit $\varepsilon = 0$, the static (frozen) variable m becomes a control parameter driving the dynamics of the fast dynamical subsystem:

$$\mathbf{v}' = F(\mathbf{v}, m). \quad (5)$$

Starting with an initial point (\mathbf{v}_0, m_0) , a trajectory of (5) converges to an attractor for the given m . Such an attractor may be a stable equilibrium state, or a stable periodic orbit when $\mathbf{v} \in R^2$, or have a more complex structure in the high-dimensional case. When the equilibrium state or the periodic orbit of the fast system is structurally stable (normally hyperbolic), it depends smoothly on m . Hence, by varying m , one can continue the smooth invariant manifolds of system (5). The manifold composed of the equilibrium states of the fast subsystem is a space curve, M_{eq} , in the extended phase space $\mathbf{v} \otimes m$ of (4). When the manifold is made of periodic orbits, it is a cylindrically shaped 2D surface, M_{lc} . Locally, a normally hyperbolic section of the manifold becomes a center manifold for (4), and hence persists in a close system (4) for small ε . This implies that solutions of (4) will stay close to such attracting segments of the manifold, which are made of stable periodic orbits or stable equilibria of the fast subsystem.

A trajectory of the system (4) at $0 < \varepsilon \ll 1$, traced down by the phase point starting from an initial point (\mathbf{v}_0, m_0) , will behave in the following way: within a finite interval of time it converges exponentially fast to the chosen attracting manifold, either M_{eq} or M_{lc} , so that its m -coordinate remains near m_0 . Once nearby, the phase point slides along the manifold with the rate of change in the m -direction of order ε . For system (3) this corresponds to a rapid jump of the \mathbf{v} -variable toward the invariant manifold followed by a finite rate evolution in m . Having approached the cylinder-shaped manifold $M_{\text{lc}}(\varepsilon)$ the phase point wraps around it in the \mathbf{v} -space. The direction of slow drift in the m -variable is determined by the slow equation averaged over the period of a turn around $M_{\text{lc}}(\varepsilon)$.

An equilibrium state of the fast system is given by the condition $F(\mathbf{v}, m) = 0$, that is, the equation of the 1D quiescent manifold M_{eq} in the (\mathbf{v}, m) -extended phase space. An equilibrium state of the full system (4) resides at the intersection point of this manifold with the *slow nullcline* $m' = 0$ given by $G = 0$. Note that the coordinates of the equilibrium state do not depend on the small parameter ε , but the stability (i.e. the characteristic exponents) does depend on ε .

To detect slow-motion manifolds we have actually used a new and practical way for their localization in the phase space of a slow–fast neuronal model. The method capitalizes on the slow–fast dissection as well as on the parameter continuation technique. Let M_{eq} be known from the consideration of the system in the singular limit. Let the screening or sweeping parameter α be introduced (even artificially) in the slow equation in (4) so that variations of α translate the slow nullcline $m' = 0$ in the phase space of the system. Then, as α is varied, the equilibrium state of the full system (4) at $\varepsilon \neq 0$ slides along M_{eq} following the slow nullcline $m' = 0$. In the case where M_{eq} is unknown, we find the manifold without need of the conventional slow–fast dissection. Hence we can identify a slow-motion quiescent manifold in the phase space of a model by applying “*slow parameter*” continuation technique. This approach is especially valuable for neuronal models of higher dimensions where slow–fast dissections could be problematic because of the presence of multiple timescales for various ionic currents involved in the dynamics. Below, we show that a similar technique can be used to locate the slow-motion manifolds comprised of periodic orbits as well.

In the first order of ε , the evolution of the m -component of the phase point along an attracting, normally hyperbolic branch $\mathbf{v} = \mathbf{v}_{\text{eq}}^s(m)$ (by virtue of the implicit function theorem for $F = 0$) of the manifold M_{eq} in the phase space of (4) is determined by the equation

$$m' = G(\mathbf{v}_{\text{eq}}^s(m), m, \alpha). \quad (6)$$

A single zero of G is the hyperbolic equilibrium state of (6). The zero can be an attractor or a repeller, that corresponds respectively to a stable or saddle equilibrium state of the full system. A slow drift of the phase point along the branch $\mathbf{v}_{\text{eq}}^s(m)$ is either limited by a stable point of (6), or the point comes close to a critical (turning) point given by $\partial F / \partial m = 0$ on the manifold. Recall that at $\varepsilon = 0$, the m -variable is a parameter in the fast system, and therefore, the critical value of m corresponds to a codimension-one saddle-node or fold bifurcation through which a pair of equilibrium states—stable and saddle—merge and vanish. The bifurcation occurs at a minimum (maximum) of m on M_{eq} , after which m may no longer decrease (increase) along M_{eq} . So, at the fold the phase point seeks a new attractor, that is, the ω -limit set of the unstable separatrix of the saddle-node equilibrium state of the fast subsystem.

The dynamics of trajectories of (4) near an attracting, normally hyperbolic segment of the 2D cylinder-shaped manifold M_{lc} is less static for $0 < \varepsilon \ll 1$. Geometrically, the 2D slow nullcline $m' = 0$ can cut transversally through M_{lc} . So, on the surface of M_{lc} below (above) the slow nullcline, the m -component of the phase point increases ($m' > 0$) (respectively, decreases as $m' < 0$). Let $\mathbf{v} = \mathbf{v}_{lc}(\mathbf{v}_0, m_0; \tau)$ be the equation of a $T(m_0)$ -periodic stable orbit of the fast subsystem (4) at some m_0 . So, if $G(\mathbf{v}_{lc}, m, \alpha) > 0$ (< 0) on M_{lc} over a period $T(m)$ of a single turn, then the phase point slides along the manifold in the direction of increasing (decreasing) m . If the opposite drifts are canceled out after a turn, then the phase point remains on the same track. This observation is formalized in the following average slow equation introduced by Pontryagin and Rodygin [27]:

$$\begin{aligned} \langle m' \rangle &= \langle G(m, \alpha) \rangle \\ &\equiv \frac{\varepsilon}{T(m)} \int_0^{T(m)} G(\mathbf{v}_{lc}(\tau; m), m, \alpha) d\tau. \end{aligned} \tag{7}$$

This equation yields a first-order approximation for the slow m -dynamics of the phase point near the (attracting) spiking manifold M_{lc} . A zero, m^* , of function $\langle G \rangle$ is an equilibrium state of the averaged system. A hyperbolic equilibrium state of (7) corresponds to a hyperbolic periodic orbit of the full system (4) on the considered section of the manifold M_{lc} . The stability (instability) of the equilibrium state, as well as that of the periodic orbit in the m -direction, is determined by the sign of the partial $\partial \langle G \rangle / \partial m$ at the given zero: if negative, then the periodic orbit is stable. If it is positive, then the orbit is of the saddle type, with 2D stable and unstable manifolds. Locally, the unstable manifold is a section of M_{lc} .

If (7) has no zeros, then the attracting segment of the manifold M_{lc} is transient for the solutions of the system that coil around M_{lc} in the direction of increasing or decreasing m , depending on whether $\langle G(m, \alpha) \rangle$ is positively or negatively defined. In context of neuronal dynamics the corresponding interneuron model is ready to burst.

4 Slow manifolds in the interneuron model

The application of the slow parameter continuation technique to the leech heart interneuron model is

demonstrated in Fig. 1. The quiescent manifold M_{eq} has a distinguishable Z-shape in the phase space of this (and many other) Hodgkin–Huxley type models. The two turning points on M_{eq} , correspond to saddle-node bifurcations in the fast subsystem where a pair of equilibrium states coalesce and vanish. In the interval between the folds the fast subsystem (5) has three equilibria. The middle segment of M_{eq} is comprised of saddles. The upper and lower branches of the nullcline M_{eq} correspond to the depolarized and hyperpolarized states of the interneuron, respectively. The hyperpolarized (solid) branch of M_{eq} is comprised of stable equilibria of the fast subsystem, and hence of the full system as well, with the given slow equation (nullcline), see Fig. 1. Again we stress that by construction, the slow manifold M_{eq} is sought as a V_{K2}^{shift} -parametric space curve in the phase space of the model.

An approach similar for finding M_{eq} is used to locate the tonic spiking manifold M_{lc} comprised of the periodic orbits. Let there exist a stable, round periodic orbit of the entire model (4) for some α (on the hypothetically known M_{lc}). Variations of α , moving the slow nullcline in the v -direction, make the periodic orbit slide along the sought manifold M_{lc} . So, by parametrically continuing the periodic orbit, we can uncover the manifold M_{lc} without a prior slow–fast dissection. Furthermore, this parameter continuation approach yields the slow manifold for a given small parameter, not an approximation in the singular limit, in contrast to the manifold M_{eq} , which is independent of ε .

4.1 Tonic spiking manifold

To reveal the tonic spiking manifold M_{lc} , we first find a stable periodic orbit corresponding to tonic spiking oscillations of the interneuron. Such as one detected in the phase space of the model at $V_{K2}^{shift} = -0.026$ V is on the edge of the sought manifold M_{lc} in Fig. 2. Next, as V_{K2}^{shift} is increased from -0.026 to 0.0018 , we follow the periodic orbit by using the software package CONTENT (freely available at <http://www.staff.science.uu.nl/~kouzn101/CONTENT/>). Approaching the latter value, the stable manifold M_{lc} folds back, wrapping around the quiescent manifold M_{eq} , and touches the low hyperpolarized fold. We stress that revealing the topology of the spiking manifold would be impossible with the slow–fast dissection [40]. Thus, by construction, the aforementioned center manifold

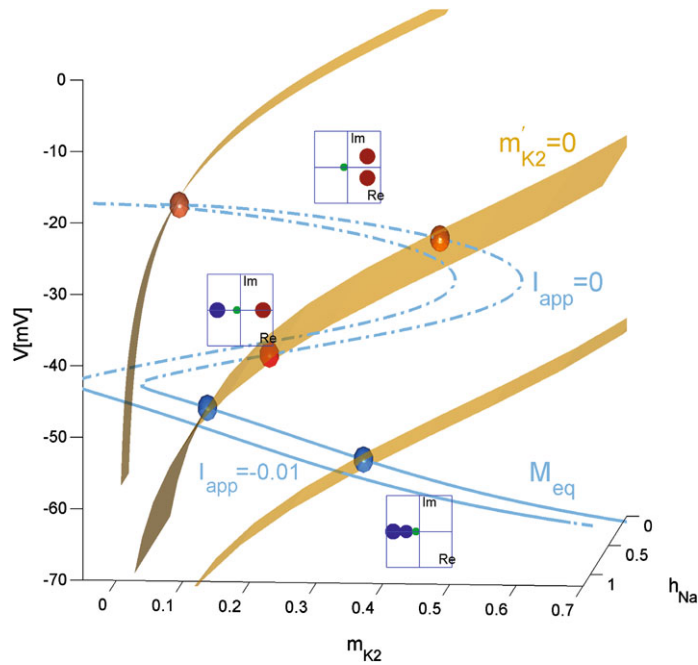


Fig. 1 The equilibrium state of (1) for the given V_{K2}^{shift} lies at an intersection point of the 1D Z-shaped quiescent manifold M_{eq} comprised of the equilibrium states of the fast subsystem with the 2D sigmoidal slow nullcline $m'_{K2} = 0$. The position of the intersection point (i.e. the equilibrium state) depends on V_{K2}^{shift} : as the parameter is varied, the slow nullcline moves

in the V -direction, thus tracing down the manifold M_{eq} . Application of the constant external current shifts M_{eq} , instead, leftwards if I_{app} is hyperpolarizing (negative). Three insets depict schematically the characteristic exponents of the typical equilibria along M_{eq}

M_{lc} is a parametrically sought two-dimensional surface foliated by a large number of the (spiking) periodic orbits of the model (1). A solution of (1) repeatedly switching between M_{eq} and M_{lc} represents bursting activity. The hyperpolarized fold on M_{eq} corresponds to the beginning of a burst. The number of complete revolutions of the solution around M_{lc} before it reaches the fold on the spiking manifold is the number of spikes per burst. We use this winding number to classify bursting regimes.

Figure 2 shows the parametric slow-motion manifolds, tonic spiking M_{lc} and quiescent M_{eq} in the 3D phase space of the interneuron model (1) as the bifurcation parameter V_{K2}^{shift} increases from -0.026 to 0.0018 . The bifurcation diagram revealing the dependence of the tonic spiking periodic orbits on the parameter V_{K2}^{shift} is shown in Fig. 3. Figure 3 shows that within the interval $V_{K2}^{shift} \in [-0.0234; -0.0259]$, the tonic spiking branch has a hysteresis, and therefore the system (1) may exhibit bistability as three periodic orbits coexist on M_{lc} , see Figs. 2 and 3.

4.2 Averaging

To investigate the bistability, we use the combination of the averaging and parameter continuation technique. Figure 4 illustrates the results obtained for the interneuron model (1). Inset A1 of the figure shows that when the slow nullcline $m' = 0$ cuts through the spiking manifold M_{lc} at negative values of the bifurcation parameter V_{K2}^{shift} , the corresponding slow average equation (7) has a single zero of $\langle G \rangle$ (Inset A2) corresponding to a stable (tonic spiking) periodic orbit (shown in green). Recall that with the slow nullcline the phase point is pushed by the flow (slow equation in (5)) so that its m -coordinate increases, or decreases otherwise. If the phase point stays on a periodic orbit, the opposite forces are canceled out on average, over the period of the orbit. This results in a circular motion of the phase point around the “center of gravity” of the periodic orbit. The (v, m) -coordinates of this

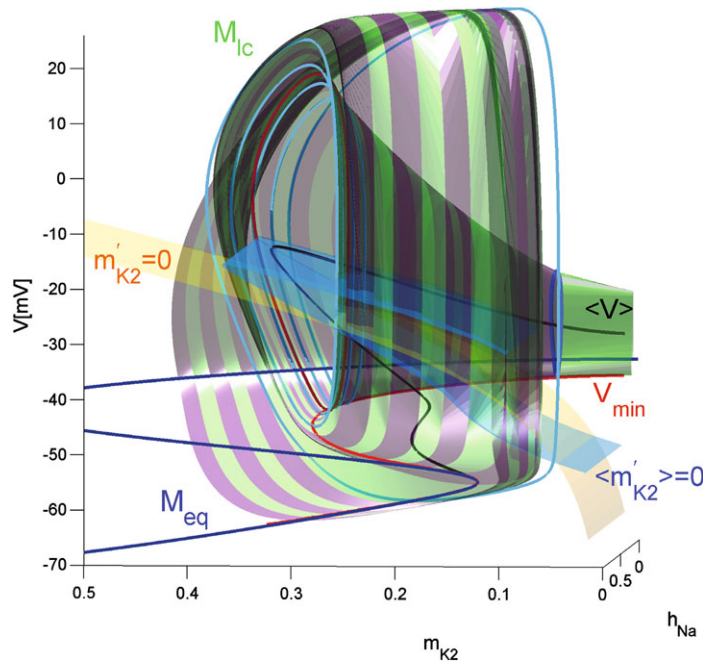


Fig. 2 (Color online) Slow-motion manifolds and nullclines of the model (1): the 2D spiking manifold M_{1c} is foliated by the periodic orbits continued, from the left to the right, as the parameter V_{K2}^{shift} is increased from -0.026 to 0.0018 . The space curves V_{min} and $\langle V \rangle$ are made of minimal and average coordinates of the periodic orbits. M_{1c} glues to the hyperpolarized fold of the quiescent manifold, M_{eq} , comprised of the equilib-

rium states of (1), where the curve of the averaged values $\langle V \rangle$ terminates. An equilibrium state of (1) is the intersection point of M_{eq} with the slow (yellow) nullcline $\dot{m}_{K2} = 0$ for the given V_{K2}^{shift} . Also shown (in red) is the curve of the v -minimal coordinate values of the periodic orbits making M_{1c} . This curve is used to define the Poincaré mapping taking it onto itself after one revolution around M_{1c}

center are given by

$$\begin{aligned} \langle \mathbf{v} \rangle &= \frac{1}{T} \int_0^T \mathbf{v}_{1c}(\tau; m) d\tau, \\ \langle m \rangle &= \frac{1}{T} \int_0^T m_{1c}(\tau; v, V_{K2}^{shift}) d\tau, \end{aligned} \tag{8}$$

where $(\mathbf{v}_{1c}, m_{1c})$ is the equation of the periodic orbit. The position of the periodic orbit on M_{1c} and the gravity center depend on where the slow nullcline $\dot{m}' = 0$ cuts through M_{1c} . By increasing the parameter V_{K2}^{shift} , the slow nullcline lowers, and the periodic orbit slides along M_{1c} in the direction of increasing m . Hence, while V_{K2}^{shift} is varied, the gravity center traces down a space curve, denoted by $\langle V \rangle$ in the figures depicting the phase space of the interneuron model, of the average coordinates of all periodic orbits forming M_{1c} . A fold of the curve $\langle V \rangle$ (Fig. 3) corresponds to a saddle-node bifurcation of periodic orbits; there are two such bifurcations occurring at $V_{K2}^{shift} = -0.0234$ and -0.0259 (Fig. 3). Note that in order to accu-

rately describe the evolution of periodic orbit one has to work with the averaged branches, as 2D projections may be misleading. For example, we can see from Fig. 3 that it is the average branch $\langle v \rangle$ that glues to the hyperpolarized fold on the quiescent manifold M_{eq} at $V_{K2}^{shift} = 0.002471$. This corresponds to a homoclinic saddle-node or SNIC bifurcation: the closer the periodic orbit approaches the equilibrium state, the longer the phase point lingers near the “ghost” of the saddle-node equilibrium state. This makes the period of the orbit greater, which implies that $\langle v \rangle$ gets closer to the v -coordinate of the bifurcating equilibrium state (fold point). Observe another peculiar feature of the $\langle v \rangle$ branch: its inflection point (labeled PD) at $V_{K2}^{shift} = -0.0249$ corresponds to a period-doubling bifurcation.

Figure 4(B1) shows that while increasing the parameter V_{K2}^{shift} makes the slow nullcline lower, the graph of $\langle G \rangle$ elevates, touching the horizontal axis. This (concave down) tangency implies a double zero of $\langle G \rangle$ that corresponds to a saddle-node bifurcation

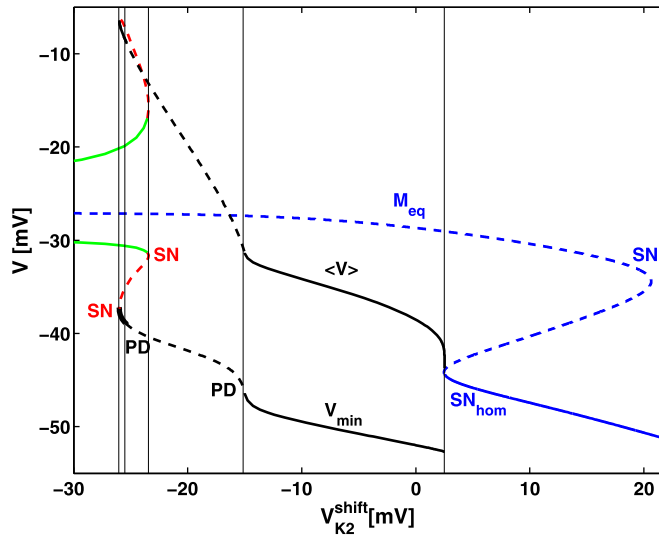


Fig. 3 Dependence of the v -coordinates of the equilibrium states (M_{eq}) and the periodic orbits (average $\langle V \rangle$ and minimal V_{min} branches) of the model on the bifurcation parameter V_{K2}^{shift} (given in millivolts here). The solid and dashed segments of M_{eq} correspond to stable and unstable equilibria. The average branch $\langle V \rangle$ terminates at the fold, SN_{hom} on M_{eq} , cor-

responding to a homoclinic saddle-node (SNIC) bifurcation at $V_{K2}^{shift} = -0.002471$. Saddle-node bifurcations of periodic orbits occur at $V_{K2}^{shift} = -0.0234$ and -0.0259 ; they are associated with two folds, SN, on $\langle V \rangle$ and V_{min} branches. The inflection point PD at -0.0149 corresponds to a period-doubling bifurcation

in the average slow equation. Decoupling the double zero at a further increase of the parameter gives rise to the appearance of two more periodic orbits on M_{lc} : stable (black) and saddle (red). In the parameter interval between -0.0259 and -0.0234 there are three periodic orbits, enough for bistability of tonic spiking oscillations in the interneuron, provided that the newborn large amplitude periodic orbit remains stable. Note that loss of the stability of the newborn periodic orbit initiates the cascade of period-doubling bifurcations in the model. The orbit will regain its stability further through a reverse period-doubling bifurcation at $V_{K2}^{shift} = -0.0149$. The spiking manifold M_{lc} continued by this large amplitude periodic orbit terminates, after it touches the hyperpolarized knee point on M_{eq} through the homoclinic saddle-node bifurcation.

As V_{K2}^{shift} is increased further, the initially stable (green) and saddle (red) periodic orbits come closer and merge through the saddle-node bifurcation at $V_{K2}^{shift} = -0.0234$ when $\langle G \rangle$ becomes quadratically tangent (concave up) to the horizontal axis again; see insets C1 and C2. After the annihilation of the stable (tonic spiking) periodic orbit, the interneuron model is ready for bursting because the attracting section of

the manifold M_{lc} is free of a transient solution for the whole range of the m_{K2} -variable.

In contrast to equilibrium states, the position of a periodic orbit on M_{lc} is determined by the slow nullcline only implicitly. The reason is that the slow equation in (1) is not linear in v ; see the Boltzmann functions ((2)) on the right-hand side of the model (1). Because of that the intersection point of 1D average branch $\langle v \rangle$ with the 2D slow nullcline surface $m' = 0$ is not the gravity center of the periodic orbit at the given V_{K2}^{shift} . To find its exact location on $\langle v \rangle$ graphically (likewise the case of equilibrium states), we proposed a new concept of the average nullclines [39, 58]. For the model under consideration, we introduce the average slow nullcline as follows: define

$$\langle m_{K2}^\infty \rangle = \frac{1}{T} \int_0^T m_{K2}^\infty(v_{lc}(\tau; v)) d\tau, \tag{9}$$

by averaging the corresponding Boltzmann function on the periodic orbit over its period at the given V_{K2}^{shift} on M_{lc} . As v_{lc} depends on V_{K2}^{shift} , by varying the parameter we find the whole range of $\langle m_{K2}^\infty \rangle$ on the periodic orbits. Observe that

$$\langle G \rangle \sim \langle m_{K2}^\infty \rangle - \langle m_{K2} \rangle.$$

The graph of the average nullcline given by $(\langle f_{m_{K2}}^\infty \rangle, \langle v \rangle)$ is a 2D cylindrical surface (blue color), labeled by $\langle m' \rangle = 0$ in Fig. 2. An intersection point of this V_{K2}^{shift} -parametric surface with the 1D V_{K2}^{shift} -parametric branch $\langle v \rangle = 0$ is the gravity center of the sought periodic orbit only provided that the point corresponds to the same value of V_{K2}^{shift} . By the construction of both $\langle m' \rangle = 0$ and $\langle v \rangle = 0$, this point is a zero of $\langle G \rangle = 0$, see Fig. 4. Thus, the geometry and mutual location of the average nullclines let one determine the number of periodic orbits, if any, on the tonic spiking manifold and saddle-node bifurcations, too; see Fig. 5

To conclude this section, we point out that the averaging method based on (7) allows for easy localization of periodic solutions around M_{Ic} , as well as it determines their stability, and predicts some local bifurcations. The limitations of the method are obvious too: these findings provide little information about the global behavior of orbits like bursting ones. Besides, consideration of a single average equation excludes, by default, all other bifurcations, that orbits may undergo, such as period-doubling, homoclinic, as well as other complex bifurcations which underlie various routes to chaos. To overcome this obstacle, further explorations of global dynamics of the interneuron model should be continued by employing Poincaré return mappings for the slow changing variable m_{K2} and for an entire interval of the fast varying voltage.

5 Poincaré mapping for slow variable

A 1D Poincaré return mapping for the slow m -variable can be defined on a 2D cross section that cuts transversely the spiking manifold M_{Ic} in a line l_{Ic} . On it, the mapping defined over periods $T(m, \alpha)$ of revolutions around the 2D cylinder-shaped manifold M_{Ic} assumes the form [42–44]:

$$m_{n+1} = m_n + \varepsilon T(m, \alpha) \langle G(m, \alpha) \rangle. \tag{10}$$

In essence, (10) is a discrete version of the averaged equation (6). Properties of (10) are determined by the product $T(m, \alpha) \langle G(m, \alpha) \rangle$, scaled with ε , provided that the mapping is not considered near the homoclinic saddle-node bifurcation (SNIC) where the revolution period around M_{Ic} grows with no bound. Indeed, it is $\langle G \rangle$ that dictates the dynamics of the mapping.

Note that in case of the square-wave bursters where the spiking manifold is terminated by a homoclinic bifurcation of the saddle of the fast subsystem, the period $T(m, \alpha)$ grows logarithmically fast, so the shape of the slow mapping is due to $T(m, \alpha)$. This results in the slow mapping assuming a unimodal shape that gives rise to a quick cascade of period-doubling bifurcations at the transition from tonic spiking into bursting [34, 35, 45, 47, 59].

To get the slow mapping for the interneuron model one needs $\langle G \rangle$ (known), the period T of the orbit as the parameter V_{K2}^{shift} is varied and $\varepsilon = 1/\tau_{m_{K2}}$. The latter is just a scaling factor which we will drop for the sake of visualization. The transformations of $\langle G \rangle$ are depicted in Fig. 4. In short, to create the slow mapping, one scales and then rotates the graph $\langle G \rangle$ through $\pi/4$ counterclockwise. The 1D mapping for the slow gating m -variable defined through the expression (10) is shown in Fig. 6. Observe that the mapping is not single-valued, because the spiking manifold M_{Ic} in the projection onto the m -coordinate folds back, which gives two branches for the mapping graph. So, its upper branch characterizes the dynamics of the slow m_{K2} -variable before the fold on the manifold M_{Ic} , while the lower branch corresponds to the segment of M_{Ic} after it turns from inside out or folds back.

Nevertheless, with some limitation we can still interpret some of its basic properties. First is that fixed points of mapping (10), located at the zeros of $\langle G \rangle$, correspond to the same periodic orbits of the model. For example, for $V_{K2}^{\text{shift}} < -0.0026$, the mapping has a single stable fixed point (green) in inset A corresponding to the stable (tonic spiking) periodic orbit centered around the depolarized level of the interneuron, see Fig. 4A. As the parameter is increased, the mapping graph touches first the bisectrix and gains two more fixed points, unstable (red) and stable (black) through the saddle-node bifurcation. The unstable point serves as a threshold dividing the basins of two attractors. Further increase of V_{K2}^{shift} to -0.0234 makes the tonic spiking and unstable (middle) fixed points merge and vanish through the secondary saddle-node bifurcation.

The use of the 1D slow mapping lets us overcome one major limit of the single average equation (6), namely, besides geometrically evident tangent or saddle-node bifurcations, we can predict where the period orbit starts a period-doubling cascade. This occurs when the slope of the mapping at the fixed point (black corresponding to a large amplitude periodic orbit in Fig. 4(C1)) becomes smaller than -1 . To avoid

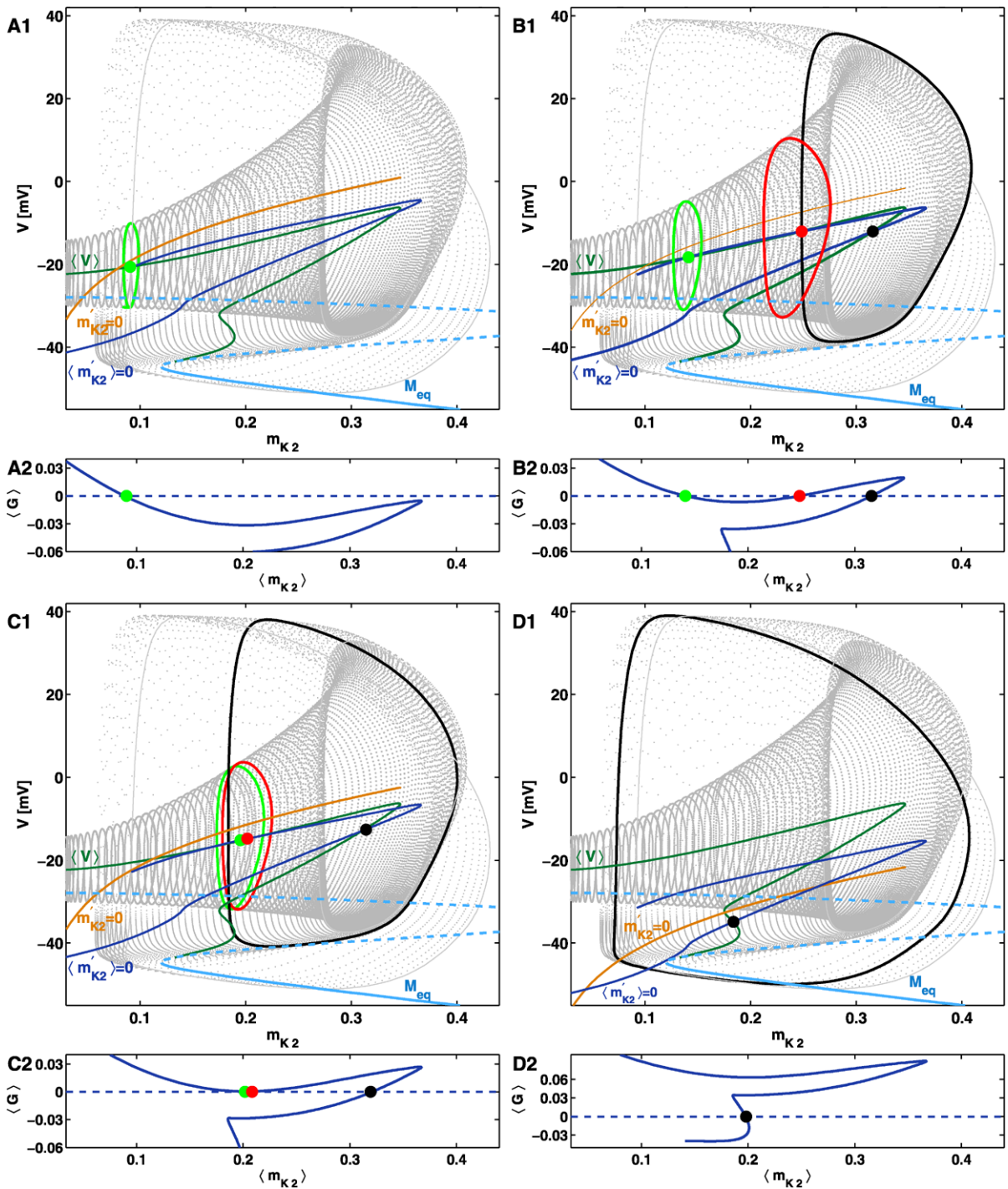


Fig. 4 (A1–D1): (v, m_{K2}) -projections of the V_{K2}^{shift} -parametric manifolds M_{eq} and M_{lc} comprised of equilibria and periodic orbits of the interneuron model (1). (A2–D2): Numerically found graphs of $\langle G \rangle$ (defined in (7)) for $V_{K2}^{shift} = \{-0.0255, -0.0245, -0.02468, -0.0207\}$: a zero of $\langle G \rangle$ corresponds to a periodic orbit of the model. Sign of $\langle G \rangle_{m_{K2}}$ de-

termines the stability of an equilibrium state (periodic orbit (in same color)) in m_{K2} . Variations of V_{K2}^{shift} make the zeros of $\langle G \rangle$ translate, as well as the periodic orbits slide along M_{lc} . A tangency of $\langle G \rangle$ (in B2) corresponds to a saddle-node bifurcation, where two corresponding periodic orbits merge and then annihilate

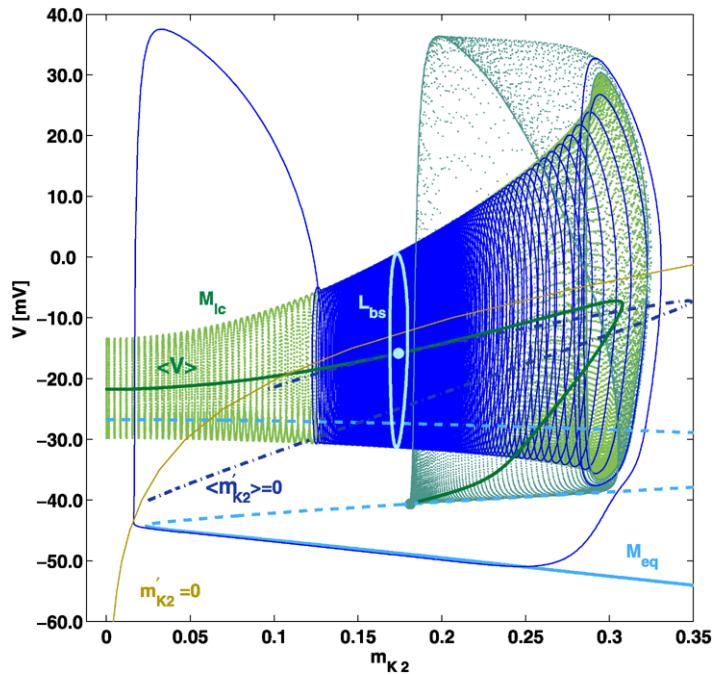


Fig. 5 (Color online) Neuron model (1) at the blue sky catastrophe at the moment of the disappearance of the stable tonic spiking periodic orbit with a saddle one on the manifold M_{LC} in the (m_{K2}, V) -projection at $V_{K2}^{shift} = -0.02452$. The blue z-shaped line, M_{eq} , consists of the equilibrium states of the fast subsystem (dotted and solid segments represent unstable and stable ones). The point of its intersection with the slow nullcline $m'_{K2} = 0$ in is a single equilibrium state. The cylinder-shaped surface $M_{LC} = M_{LC}^s \cup M_{LC}^u$ is comprised of the tonic spiking

periodic orbits of the model. The (green) curve $\langle V \rangle$ shows the dependence of the v -coordinate of the periodic orbits, averaged over the period, on m_{K2} . The dashed (blue) curve is the average nullcline $\langle m'_{K2} \rangle = 0$. The contact point between $\langle V \rangle$ and $\langle m'_{K2} \rangle = 0$ corresponds to the saddle-node periodic orbit, L_{bs} . A section of M_{LC}^s on the right from the saddle-node periodic orbit L_{bs} is locally its unstable manifold, W^u . Shown in red is a trajectory homoclinic to L_{bs} that becomes a stable orbit bursting as after L_{bs} disappears

repetitions, we finish a rather limited consideration of the bi-valued return mapping for the slow dynamics of the interneuron model (1) and turn our attention to a more informative mapping for the fast voltage. Such fast mappings are more natural for neuroscience applications, as the membrane potential v is truly the only variable that is directly measured in experimental studies.

Let us conclude this section with the following remarks concerning the Poincaré return mapping for slow variables in neuron models:

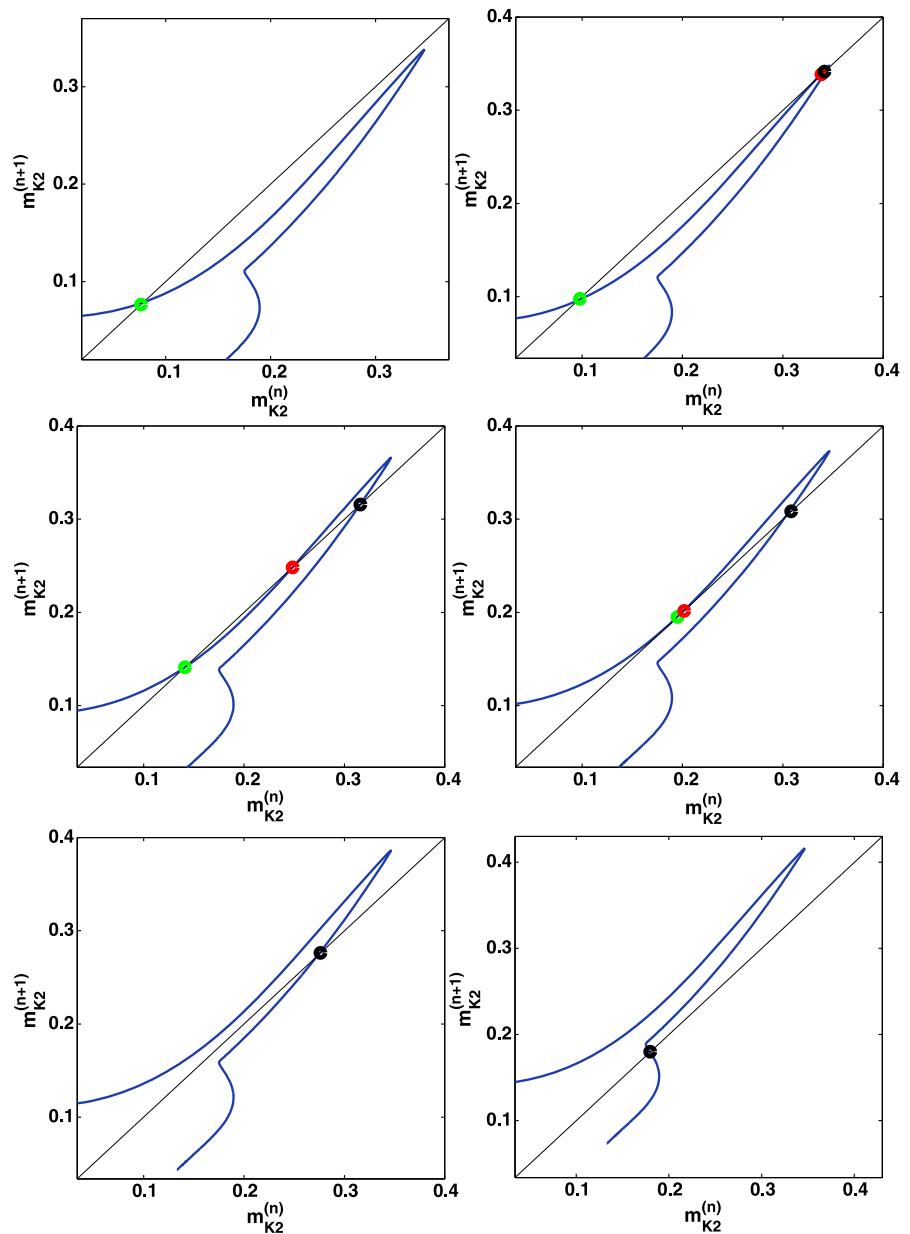
- Pros: the mapping is simply evaluated from (10) provided that its right-hand side is known a priori. The mapping allows for easy detecting a tangent or saddle-node bifurcation, and is helpful for identifying period-doubling bifurcations.
- Cons: The slow mapping is no single-valued one for the model in question, and also for many models

with folded tonic spiking manifolds, like in elliptic bursters. Because of that, a proper interpretation of the mapping and bifurcations of fixed points can be problematic. The major concern is that the implementation and realization of such mappings for slow gating variables, which seem so natural and doable in numerical studies, are hard to compare to or justify in experimental studies where the voltage remains the only measurable variable, excluding models with slowly varying calcium concentrations.

6 Poincaré map for fast membrane potential

One may wonder about the conditions under which the neuron starts to burst, and how this bursting activity evolves into tonic spiking activity as the control parameter is varied. An evident observation that

Fig. 6 (Color online) Bifurcation stages of the 1D Poincaré mapping for the slow m_{K2} -variable as V_{K2}^{shift} is increased from -0.0255 to -0.0018 . The mapping is not single-valued one due to the fold on the tonic spiking manifold M_{IC} . Fixed points correspond to periodic orbits (shown in same color in Fig. 4) of the interneuron model (1); the stable (green) fixed one corresponds to periodic tonic spiking activity. The fixed points emerge and vanish through the tangent or saddle-node bifurcations



both tonic spiking and bursting activities have oscillatory character lets one take full advantage of the technique of Poincaré return mappings to reveal the hidden mechanisms governing transitions between activities. To do this in a straightforward manner, one needs a long trace to identify a sequence of successive, local minimal values of V in it. Then, a one-dimensional point-wise mapping, T , can be defined as follows: $T : V_n \rightarrow V_{n+1}$, where (V_n, V_{n+1}) is a pair of the consecutive minimums in the trace. All such pairs

will then form the graph of the mapping. Clearly the more such distinct pairs in the trace, the more “continuous” and informative the mapping will be. A drawback of mappings constructed from time series is their sparseness, as they reflect only dominating attractors of a system.

In this section, we discuss the numerical algorithm for constructing a one-parameter family of 1D Poincaré return mappings taking a voltage interval into itself in Hodgkin–Huxley neuronal models. The ap-

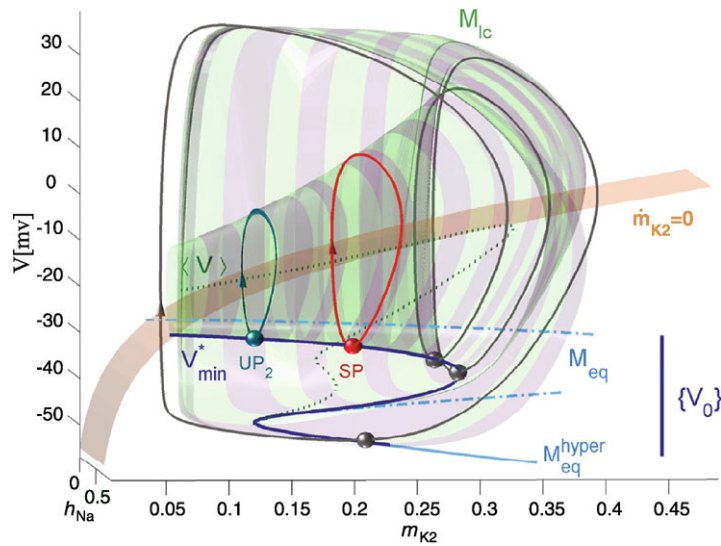


Fig. 7 Space curve V_{\min}^* on the bottom of the tonic spiking manifold M_{lc} is employed as initial data to generate the outgoing trajectories that define the Poincaré mapping taking V_{\min}^* into itself after a single revolution around M_{lc} . An initial point returning to itself after a single or several turns around M_{lc} , is a

fixed point (labeled by spheres UP_2 and SP), or forms a periodic orbit (three gray spheres) of the mapping, respectively. The set $\{V_0\}$ is made of the V -minimal coordinates (on V_{\min}^*) of the periodic orbits foliating M_{lc}

proach was first proposed for the model under consideration in [41, 49, 50] and enhanced for elliptic bursters in [51]. Such mappings let us find and examine not only stable, but unstable solutions of the system as well. Using the onto mappings we can conduct a thorough study of bursting and its bifurcations en route to tonic spiking in the interneuron model (1). This approach is broadly applicable to most slow-fast neuronal models as it capitalizes on the fact that the solutions of such system linger around the slow-motion manifold of low dimensions.

The first stage in the mapping construction begins with the localization of the tonic spiking manifold M_{lc} , such as those shown in Figs. 1 and 7. Next we single out a space curve, V_{\min} on the manifold, that corresponds to minimal (maximal) voltage values (denoted by V_0) for all periodic orbits constituting M_{lc} . The return mapping is defined to take this curve onto itself after a single turn around M_{lc} . Practically, the points $\{V_0\}$ are used as the initial conditions for the numerically integrated outgoing solutions of the model (1). The integration of every such solution is stopped when it reaches the successive minimal value V_1 . The found pairs, (V_0, V_1) , constitute the graph of the Poincaré mapping for selected values of the control parameter, V_{K2}^{shift} shown in Fig. 7.

The V_{K2}^{shift} -parameter family of the Poincaré mappings for a voltage interval is shown in Fig. 8; here, we set $\tau_{K2} = 0.25$ and $I_{pol} = 0$. The mappings are called *unimodal* because of a single critical point [66]. Such non-invertible mappings have several peculiar features, including, for example, homoclinic orbits to repelling fixed points [67] which give rise to the onset of chaotic dynamics in a system. The “continuity” (6000 points forming the graph) of the mappings allow for the detection of fixed and periodic attractors and repellers. Such unstable orbits, including homoclinic and heteroclinic, are the hidden organizing centers globally governing the dynamics of a model. Using the voltage mappings we can analyze all local and global bifurcations of periodic and aperiodic orbits, including saddle-node and period-doubling bifurcations, spike adding, inner crisis within bursting, etc. Chaotic dynamics can now be explored by means of the symbolic description based on the theory of kneading invariants [68, 69], and the topological entropy as a quantitative measure of bursting complexity in the model. Besides, we can examine the boundaries of multistability in the model where bursting coexists with other oscillatory types of neural activity.

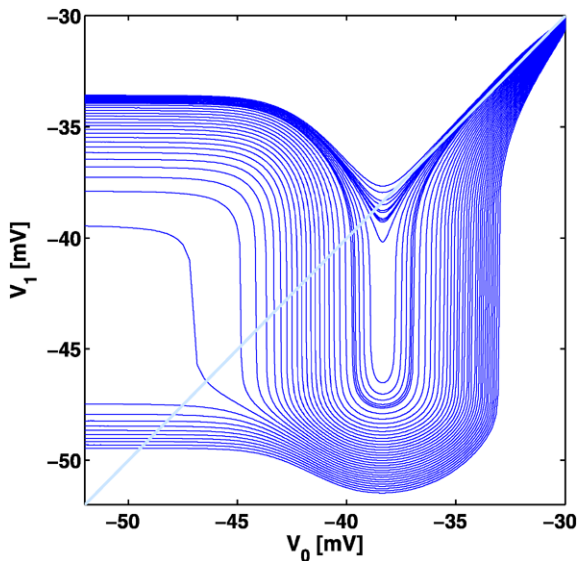


Fig. 8 V_{K2}^{shift} -parameter family of onto unimodal Poincaré mappings for the membrane potential v . A crossing point of the graph of the mapping with a 45° -line, is a fixed point corresponding to a single V -minimum of a (round) periodic orbit on the manifold M_{lc} in the phase space of the model. When the shape of the mapping graph (lower-left section) changes from concave-down to concave-up, the fixed point at the inflection point changes stability, undergoing a period-doubling bifurcation when its multiplier becomes less than -1 . A tangency of the graph with the 45° -line corresponds a saddle-node bifurcation through which two fixed points merge and vanish

7 Period doubling to bursting

A cascade of period-doubling or flip bifurcations is one of typical routes to deterministic chaos in dissipative systems. Neuronal models are no exceptions. Period-doubling bifurcations have been reported frequently in neurodynamics, especially near transitions from tonic spiking to bursting in square-wave and elliptic bursters, see [35, 36, 40, 51, 57, 59, 70] and references therein. In this section we will demonstrate how the period-doubling cascade shapes the bistable dynamics of the leech heart interneuron [39, 40].

At this point, we return to the bifurcation diagram in Fig. 3 and the phase portraits in Fig. 4, where the periodic orbits emerge and vanish as double zeros of the average equation illustrated in inset (A2–D2). Two folds on the branch of the periodic orbits plotted against the parameter, which form a hysteresis, indicate that the model can have two coexisting periodic orbits. This situation is reflected in the occurrence of two tangent, saddle-node bifurcations involving the upper branches of the voltage mappings in Fig. 8.

In what follows below, we will concentrate our consideration of the evolution of the large amplitude periodic orbit near the fold of the tonic spiking manifold, through the examination of bifurcations of the corresponding fixed point at low-value of the voltage (-40 mV). The stable periodic orbit and the mapping at $V_{K2}^{\text{shift}} = -0.0257$ are shown in Fig. 9. Recall that, by construction, the mapping describes the temporal evolutions of the minimal values of the membrane potential. Therefore, a single v -minimum of the stable periodic orbit of the model corresponds to a stable fixed point of the mapping.

This fixed point becomes unstable when the slope of the mapping graph becomes less than -1 at the fixed point on the bisectrix. This flip bifurcation gives rise to the emergence of a new period-2 orbit of the mapping, see Fig. 10. The two points of the orbit correspond to the two v -minima of the periodic orbit of the doubled period in the phase space of the interneuron model. The voltage trace starts showing the onset of spiking duplets. The bifurcation originates a forward period-doubling cascade that leads to bursting oscillations as the parameter V_{K2}^{shift} is increased. As the parameter is increased further, the period-doubling bifurcations occur more often and the model starts generating first spiking quadruplets of period-4 (Fig. 11), then octuplets and so forth.

Since following the successive periodic doubling bifurcations of the more complex periodic orbits in the phase space of the model is a graphically challenging task, we can now turn to the voltage interval Poincaré mappings to examine the evolution of dynamics, and underlying bifurcations. The next two steps in the period-doubling cascade that tonic spiking undergoes en route toward bursting, are shown in Fig. 12 depicting the period-8 and period 16 attractors.

We skip the intermediate steps of the period-doubling cascade and show a terminal phase when the model demonstrate a chaotic tonic spiking activity, Fig. 13. We use “spiking” here as the solutions of the model have not reached the hyperpolarized branch of the slow-motion manifold M_{eq} . Below it will be shown that this chaotic spiking coexists with another periodic tonic spiking that is represented by a stable periodic orbit at some inactivated values of the potassium current m_{K2} , see Fig. 4.

To conclude the examination of the period-doubling cascade, we present two bifurcation diagrams in Fig. 14. While the upper panel shows the dependence

Fig. 9 A single v -minimum of the stable tonic spiking periodic orbit in (A) on the tonic spiking manifold M_{Lc} at $V_{K2}^{shift} = -0.0257$ corresponding to a stable fixed point of the Poincaré voltage mapping in (B). (C) and (D) show the voltage trace of the model and the magnification of the voltage (constant) minimums plotted versus time

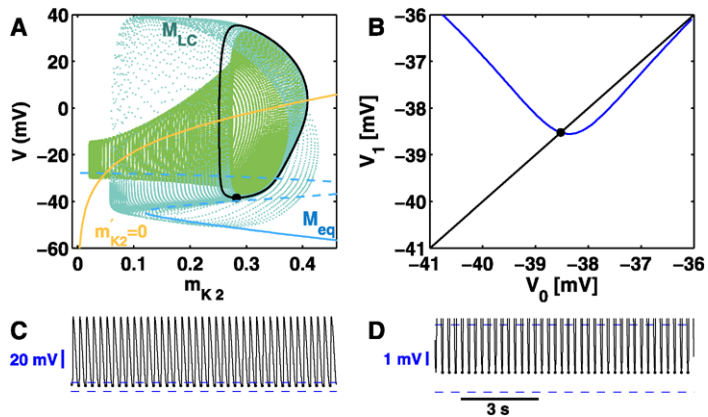


Fig. 10 (A) Stable duplet-spiking orbit at $V_{K2}^{shift} = -0.02555$ corresponding to the stable period-2 cycle of the mapping. Insets (C) and (D) show the voltage waveforms

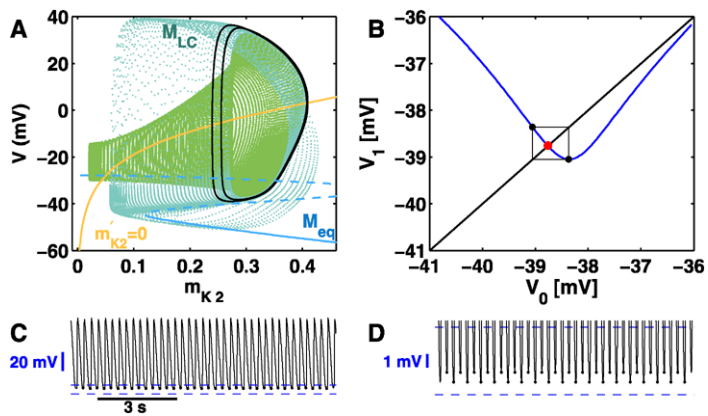
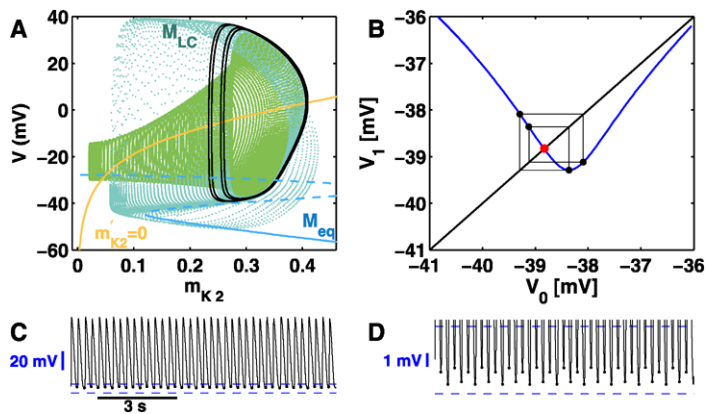


Fig. 11 Four v -minimums of the stable spiking periodic orbit spiking at $V_{K2}^{shift} = 0.0255$ corresponding to the period-4 orbit of the Poincaré mapping. Insets (C) and (D) show the voltage waveforms



of the interspike interval in the voltage traces of the leech heart interneuron model (1), the bottom panel shows the dependence of the v -coordinate of attractors of the Poincaré mapping on the parameter V_{K2}^{shift} . One can see that both diagrams agree exceptionally well. It is evident that even though constructing such return mappings is computationally expensive, nev-

ertheless the interval mappings provide high resolution details for bifurcation mechanisms underlying the transitions between various kinds of oscillatory activity in the model.

The examination of the mappings allows for making predictions about transitions that have not yet occurred in the flow. For example, it is seen from both

Fig. 12 Period-8 and period-16 spiking orbits of the voltage interval mapping at $V_{K2}^{shift} = -0.025495$ and $V_{K2}^{shift} = -0.0254948$, respectively

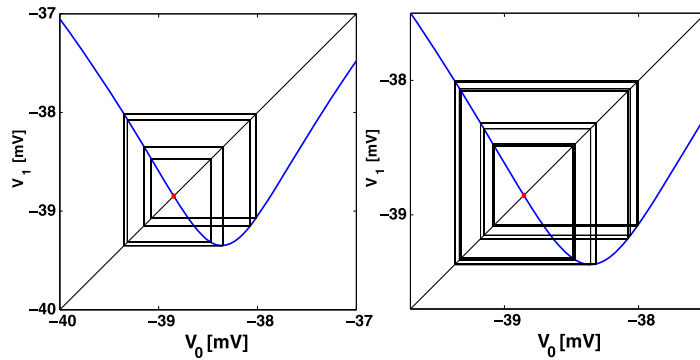


Fig. 13 Chaotic spiking of the model and in the mapping at $V_{K2}^{shift} = -0.0254$. Inset (C) show that durations of burst trains and the spike number per a train vary irregularly in the voltage trace

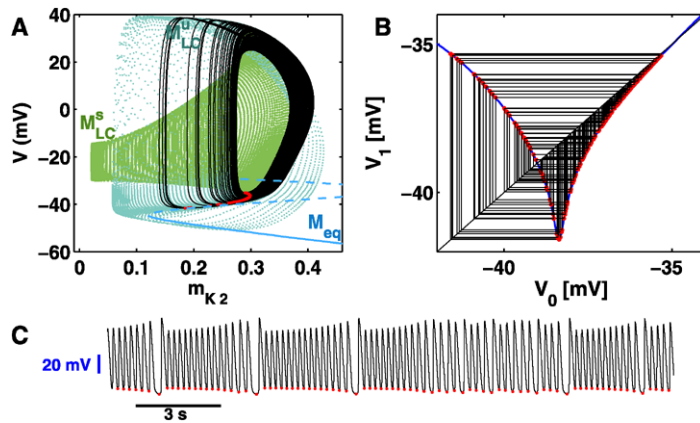
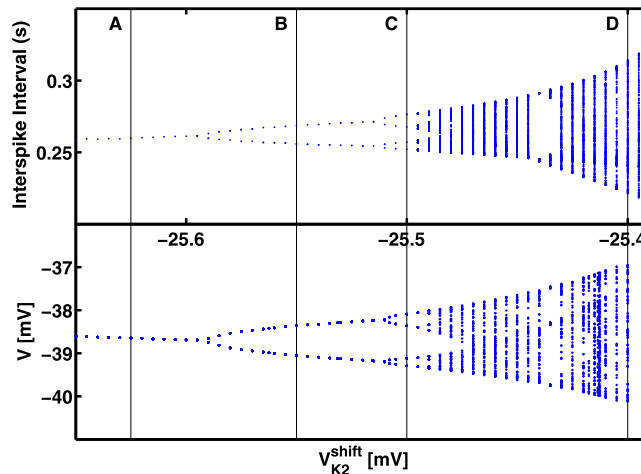


Fig. 14 (Top) Dependence of the interspike interval of the spiking solutions of the model (1) on V_{K2}^{shift} . (Bottom) The V -coordinate of the attractors of the Poincaré mapping is plotted against the parameter V_{K2}^{shift}



bifurcation diagrams that the model and the mapping demonstrate that within chaos there is the stability window, around $V_{K2}^{shift} = -0.02545$, with a stable periodic orbit inside corresponding to spiking triplets. Such a triplet corresponds to a period-3 orbit in the mapping. Use of the computationally dense mappings of the voltage interval lets one identify such an orbit as

it is made of the three fixed points of the corresponding mapping T^3 of degree-3, shown in Fig. 15. It is well known from the theory of one-dimensional mappings that such a period-three orbit is an indicator of chaotic dynamics, or “period-3 implies chaos” by Li and Yorke [71]. Moreover, in virtue of Sharkovsky ordering that if mapping has a period-3 orbit, then it has

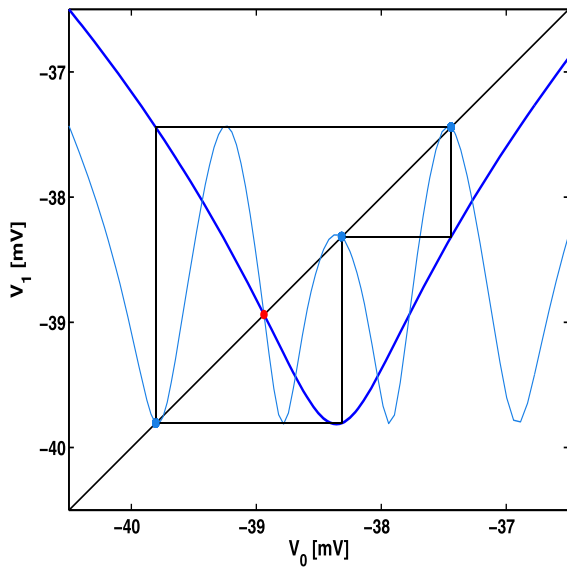


Fig. 15 (Color online) Points of the period-3 spiking orbit in the mapping (light curve) at $V_{K2}^{shift} = -0.025435$ are the fixed points of the mapping (superimposed light blue graph) of degree-3

possessed all admissible orbits of all other periods as well [66].

7.1 Symbolic description: kneadings and entropy

The period-doubling cascade ends up with the onset of spiking chaotic dynamics in the model around $V_{K2}^{shift} = -0.025475$. One way of knowing that the period-doubling cascade is over and that the chaotic dynamics being observed in the mapping and in the model is due to other contributing factors, is to identify homoclinic bifurcations which involve the fixed point initiating the cascade. The detection of homoclinic orbits of saddle periodic orbits in the phase space of even a 3D system is the state of the art. The use of the voltage mappings simplifies the search drastically as capitalizes on a particular property of the unimodal mapping [66, 67]. Namely, such an orbit can be detected by following a finite number of forward iterates of the only critical point. This critical point makes the mapping non-invertible because some of the mapping points have two pre-images, i.e., one pre-image on each monotonic segments of the mapping graph. In restriction to the left (decreasing) segment of the mapping graph the unstable fixed point UP_1 will be attracted for backward iterates of the critical point which converge exponentially fast to it as time increases. On

the other hand, since the fixed point is unstable, some finite forward iterates of the critical point can only jump onto the fixed point. This number defines the ordering number for the primary homoclinic orbit. The occurrence of a homoclinic orbit gives rise to the abundance of other homoclinics [63]. This phenomenon, known as a homoclinic explosion [42, 43], leads to deterministic chaotic dynamics in a system.

In order to quantify the degree of chaos in an 1D mapping $v_{n+1} = f(v_n)$, one can evaluate the Lyapunov exponent given by

$$\lambda = \lim_{n \rightarrow +\infty} \frac{1}{n} \log \left| \frac{df^n(v_c)}{dv} \right|,$$

where $f^n(v_c)$ stands for the n th iterate of the critical point, or any other initial point. The Lyapunov exponent for the homoclinic chaotic dynamics shown at $V_{K2}^{shift} = -0.025475$ depicted in Fig. 16 is $\lambda = 0.22$, compared to $\lambda = 0.18$ corresponding to chaos at the terminal phase of the period-doubling cascade (not shown). The fact that the system has homoclinic orbits implies a positiveness of the topological entropy. The topological entropy for 1D unimodal mappings can be estimated by means of a symbolic description with the employment of kneading invariants [68, 69].

The forward iterates of the critical point v_c of the mapping define the unsigned kneadings as follows:

$$\tilde{\kappa}_j(f^j(v_c)) = \begin{cases} -1 & \text{if } v < v_c, \\ +1 & \text{if } v > v_c, \end{cases} \tag{11}$$

i.e. basically whether the j th iterate of the critical point lands on the descending (-1) or ascending segment of the mapping graph. The kneading invariant is introduced as a sequence $\{\kappa_n\}$, where κ_n is the signed kneadings such as

$$\kappa_n = \prod_{j=1}^n \tilde{\kappa}_j, \quad \text{or} \quad \kappa_n = \tilde{\kappa}_n \kappa_{n-1}, \tag{12}$$

i.e. κ_n depends on the iterate number n as well. Next define a formal power series

$$P(s) = \sum_{n=0}^{\infty} \kappa_n s^n. \tag{13}$$

A smallest zero s_{min} of $P_n(s)$ on $s \in (0, 1)$, if any, yields the typological entropy $h = |\log(s_{min})|$.

Consider the mapping at $V_{K2}^{shift} = -0.02542$ shown in Fig. 16. The first 10 signed kneadings $\{-1, +1, +1,$

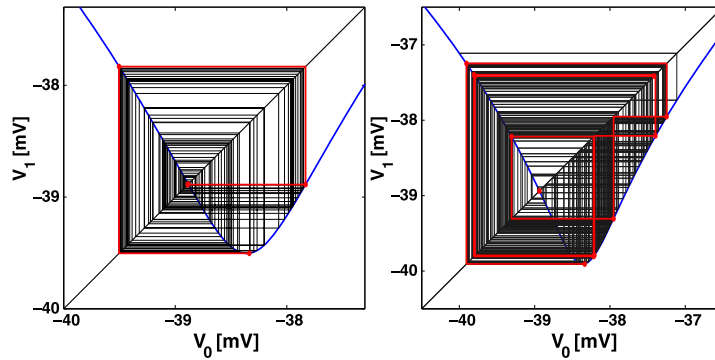


Fig. 16 (Color online) (Top) Chaos in the mapping near the primary homoclinic bifurcation at $V_{K2}^{shift} = -0.2547$ that involved the original fixed point that initiated the period-doubling cascade in the non-invertible mapping. Shown in red are the for-

ward iterates (connected) of the critical point ending at the repeller after two steps. (Bottom) Chaotic spiking at $V_{K2}^{shift} = -0.025375$. Iterates (red) of the critical point define the kneading invariants for the symbolic description of the mapping

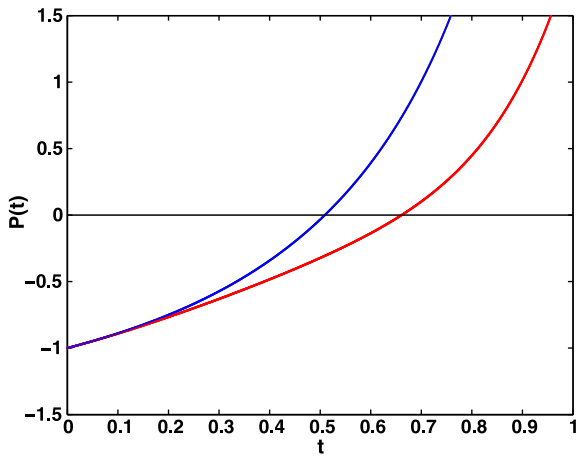


Fig. 17 (Color online) Graphs (blue and red) of the kneading invariant polynomials P_{10} for the mappings at $V_{K2}^{shift} = -0.025375$ and -0.025475 , respectively

$\{+1, +1, +1, -1, +1, +1, +1, +1\}$ give the polynomial P_{10} , the graph of which is shown in Fig. 17. The only zero of the polynomial gives the topological entropy $h = 0.32$, whereas the Lyapunov exponent for the same mappings is about $\lambda = 0.34$; $h = 0.19$ for the mapping with the primary homoclinics at $V_{K2}^{shift} = -0.025475$.

8 Bistability

In this section we discuss the kinds of bistability that the reduced leech heart interneuron model can exhibit. Use of the onto mapping makes the explanation of the

bistability especially clear. This is illustrated in Fig. 18 showing the coexisting spiking and bursting orbits (A) along with corresponding Poincaré mapping (B) and voltage traces (C, D). Decreasing V_{K2}^{shift} elevates the slow nullcline $\dot{m}_{K2} = 0$ thereby bringing it closer to the spiking manifold M_{1c} . This results in that the m_{K2} -component of the phase point slows down so that it can make extra turns around the spiking manifold M_{1c} . Moreover, a further elevation of the slow nullcline can make the middle section of the spiking manifold M_{1c} non-transitive for solutions of the model. The cause for that is the saddle-node bifurcation leading to emergence of two more periodic orbits (stable and saddle) on the spiking manifold. The saddle-node bifurcation, also called the tangent bifurcation for one-dimensional mappings, occurs when the graph of the mapping becomes tangent to the 45° line. The newly formed unstable fixed point separates the basins of attraction of bursting and tonic spiking that coexist in the model.

Since bursting is a two-times scale phenomenon due to the alternation of fast tonic spiking and slow quiescent phases, the period of bursting is the sum of the burst duration τ_{bd} and the interburst interval τ_{ij} . These times can be controlled independently. Clearly the duration (as well the number of spikes) of bursting is the longer, the closer the slow nullcline $m' = 0$ is to the corresponding tonic spiking M_{1c} . On the other hand, the interburst interval is the longer, the closer slow nullcline $m' = 0$ is to the hyperpolarized fold of the quiescent manifold M_{eq} . In other words, by varying the bifurcation parameter between two critical values corresponding to the saddle-node bifurcations for

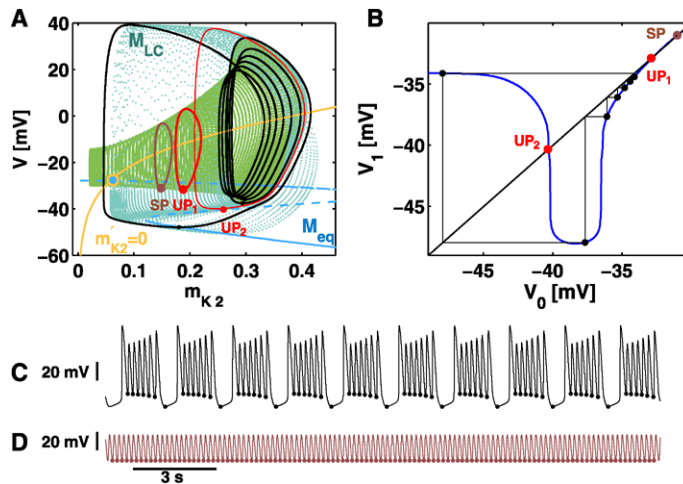


Fig. 18 (Color online) Seven-spike bursting orbit (*black*) co-existing with the tonic spiking orbit (*blue*) in the phase space of the model (1) at $V_{K2}^{shift} = -0.024$ and $\tau_{K2} = 0.25$ (panel A). Shown *in red* are the saddle periodic orbits corresponding to fixed points UP_1 and UP_2 that separated the basin of attraction of the tonic spiking and bursting orbits. Panels C and D show 7 action potential bursting and tonic spiking voltage traces, the

minimums of which form the periodic orbit and the stable fixed point (SP) in the corresponding Poincaré mapping (panel B). The stable fixed point SP emerges through a saddle-node bifurcation on the spiking manifold M_{lc} along with another unstable fixed point, UP_2 , that separates the basin of attraction of tonic spiking and bursting

periodic orbits and equilibria, respectively, we can balance out both τ_{bd} and τ_{ii} to set a particular value for the duty cycle of bursting: $DC = \tau_{bd}/(\tau_{bd} + \tau_{ii})$. So, if the interneuron is too depolarized, it will likely produce the tonic spiking activity at the lower V_{K2}^{shift} -values, while at larger values it will go into the hyperpolarized quiescent state. While V_{K2}^{shift} is an intrinsic bifurcation parameter of the model, we can treat an external applied current I_{app} in (1) as the external second parameter. In the essence, I_{app} moves the slow-motion manifolds horizontally in the (m_{K2}, v) -projection of the phase space of the model because it is introduced in the fast voltage equation, in contrast to variations V_{K2}^{shift} that keep the manifolds intact but translate the slow nullcline, $m'_{K2} = 0$, in the v -direction.

Figure 19 shows the $(V_{K2}^{shift}, I_{app})$ -bifurcation diagram of the model. In this parameter space we have singled out the zones of activity of the interneuron: bursting, quiescence, and tonic spiking. It follows from this diagram that the interneuron is locked down at the hyperpolarized quiescent state when V_{K2}^{shift} is too large; this corresponds to the blocked potassium current, i.e. m_{K2} is close to 0. When the interneuron is locked down, there is a stable equilibrium state on the hyperpolarized branch of the 1D quiescent manifold M_{eq} at an intersection point with the 2D slow null-

cline $m'_{K2} = 0$. It is evident that the external inhibitory current facilitates this state as well. In contrast, a positive excitatory current releases the interneuron from the locked depolarized state. The central part of the bifurcation diagram is occupied by bursting. The bifurcation curve SN_{eq} , corresponding to the saddle-node bifurcation, separates the bursting and hyperpolarized quiescence zones. Near the boundary, the interburst interval is long, while the burst duration is short, i.e. the duty cycle is small. This is a universal feature of the saddle-node bifurcation near which the dwelling time (read the interburst interval) throughout the phantom of the vanished saddle-node equilibrium state is scaled as $1/\sqrt{\alpha}$, where α is the distance to the bifurcation curve SN_{eq} in the bursting zone (Fig. 19).

The boundary between bursting and tonic spiking is composite consisting of two branches labeled by BSC and HB_{lc} . The first one is due to the blue sky catastrophe that describes a homoclinic bifurcation of a saddle-node periodic orbit; for details see [42–44, 58, 72]. This bifurcation, taking place on the bifurcation curve SN_{lc} , leads to the emergence of the two periodic orbits, saddle and stable, on the tonic spiking manifold, M_{lc} . The homoclinic structure of the blue sky catastrophe is due to re-injection of the phase point back into the spiking phase after it has completed a slow drifting along the hyperpolarized branch

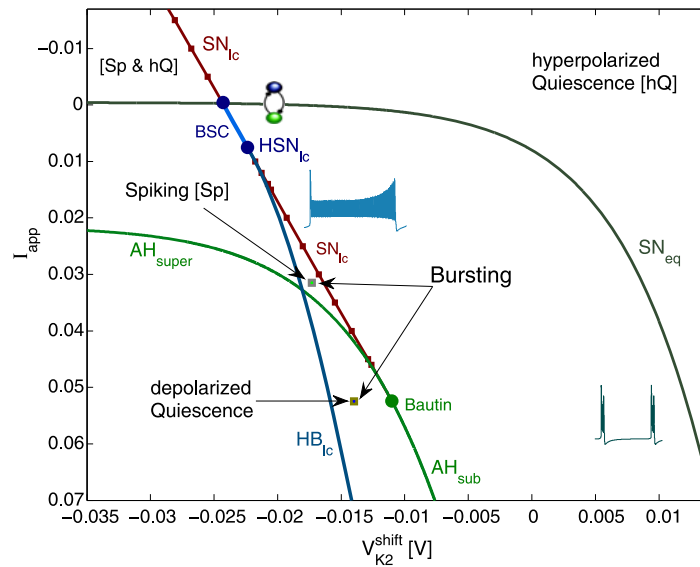


Fig. 19 $(V_{K2}^{shift}, \langle I_{syn} \rangle)$ -bifurcation plane showing the zones of activity of the model (1). Above the boundary SN_{eq} the interneuron is locked down at the hyperpolarized state. Bursting takes place between the bifurcation curves $BSC \cup HB_{lc}$ and SN_{eq} . To the left of SN_{lc} , the interneuron fires tonically. The spiking zone is bounded below by the boundary AH , underneath

which the neuron is constantly depolarized. At a codimension-two *Bautin* bifurcation the Andronov–Hopf bifurcation changes from super- to sub-critical. The wedge between SN_{lc} , HB_{lc} and AH_{super} corresponds to the coexistence of bursting and tonic spiking (Fig. 18), or the depolarized quiescence. The model is a monoactively tonic spiking state on the left from HB_{lc}

of the quiescent manifold, M_{eq} . Likewise all saddle-node bifurcations, because of the slow passage of the phase point throughout the “phantom” of the vanished saddle-node orbit, the number of spikes within the burst can be arbitrarily large near this boundary. This makes the burst duration, as well as the period of the bursting orbit, arbitrarily long (Fig. 20).

While the blue sky catastrophe describes a continuous and reversible mechanism of the transition between bursting and tonic spiking, the transition through the other section BSC of the boundary HB_{lc} gives rise to the onset of the bistability in the model, which was described above in this section. Within the wedge bounded by these curves, the tonic spiking and the bursting attractors coexist. Their basins of attraction are separated by the stable manifold of the saddle periodic orbit, which has emerged, along with the stable periodic orbit, to the left from SN_{lc} after the saddle-node bifurcation. The burst period, or more exactly the duration τ_{bd} of bursting, becomes longer the closer the bursting orbit approaches this separating saddle periodic orbit. As in all homoclinic cases, the burst duration obeys the scaling law $\tau_{bd} \sim |\log(\alpha)|$, where α is the parameter deviation from the homoclinic bifurcation.

Next, we show how the temporary characteristics, the number of spikes, burst duration, duty cycle, etc., of bursting can be employed to create bifurcation diagrams like the one shown in Fig. 19. Figure 21 is such a diagram showing the number of spikes (action potentials) per burst as a function of the parameters of the model. The color scale of the right is the number running from 0 (blue), i.e. quiescence, to 15 (red), corresponding to long bursting. One can see the perfect agreement between the bifurcation diagram in Fig. 18 and this neuroscience plausible diagram. Moreover, the latter clearly indicates the boundaries of the spike-adding sequence in the model [49].

Thus, the reduced interneuron model demonstrates three types of bistability: (A) bursting and depolarized quiescence, (B) tonic spiking and bursting, and (C) tonic spiking and hyperpolarized quiescence. What makes the bistability observable is that we can selectively choose any specific activity type, as well as robustly switch between the activity types by applying an external pulse, positive or negative, to the interneuron. This approach is demonstrated in action in Fig. 22.

Fig. 20 Temporal characteristics of bursting plotted against the bifurcation parameter V_{K2}^{shift} . The burst period increases alone with either the increase of the interburst interval due the homoclinic saddle-node bifurcation at the hyperpolarized fold near the boundary SN_{eq} , or the increase of the burst duration due to the blue sky catastrophe, or through the homoclinic bifurcation of the saddle periodic orbit near the boundary SN_{lc}

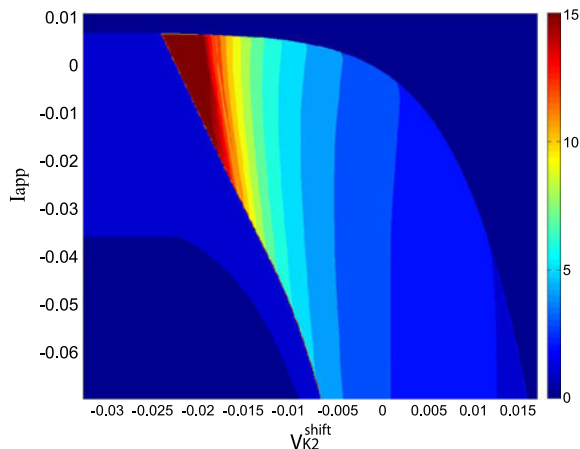
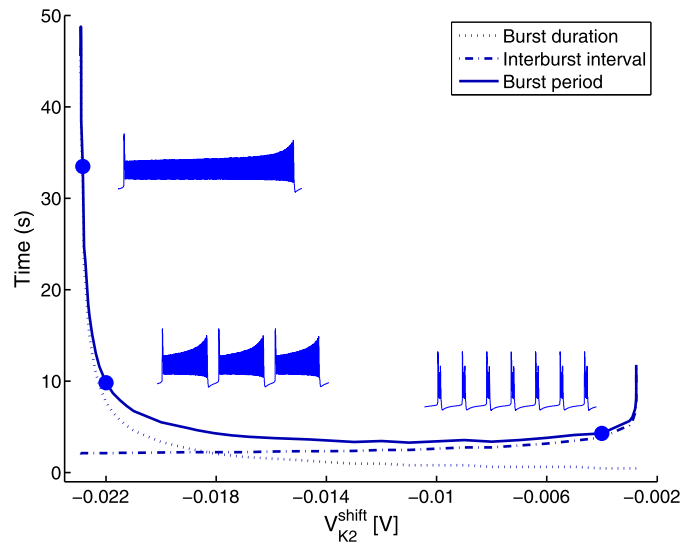


Fig. 21 (Color online) In addition to the activity zones for spiking, quiescence and bursting, $(V_{K2}^{shift}, I_{app})$ -biparametric screening plane reveals clearly the stages of the spike-adding cascade [50] and singles out regions of resistantly constant spike numbers within bursts in the model. The color bar on the right for the spike numbers per burst is scaled from 0 (blue) to 15 (red) [73]

9 Conclusions

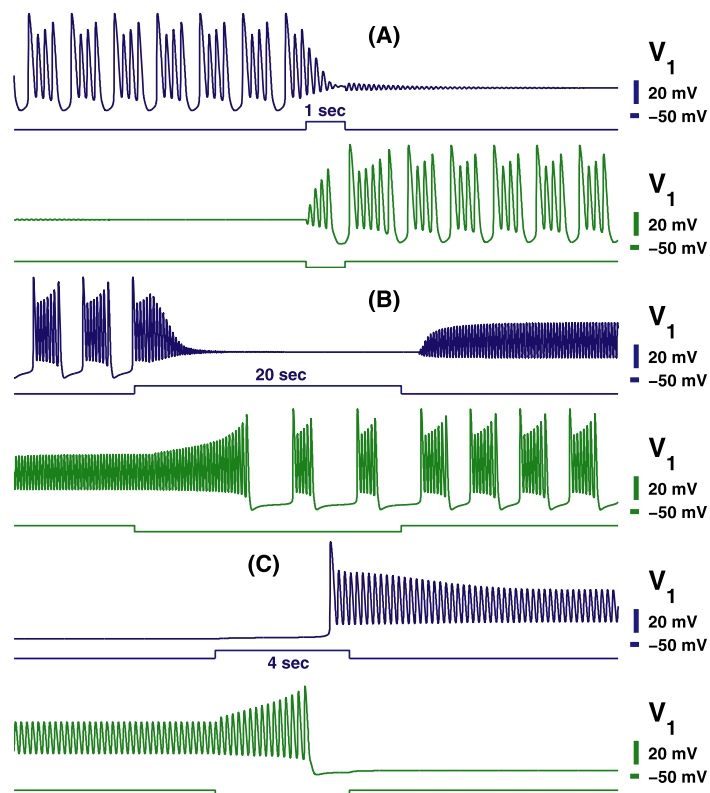
This paper compliments the findings in this dynamically rich interneuron model that have been reported by the author and his co-authors in the series of the earlier papers on the blue sky catastrophe, bistability of two types of tonic spiking, the coexistence of quiescence, tonic spiking and bursting, the spike-adding cascade toward bursting, and the sensitivity of bursting patterns to ionic channel noise, as well as mod-

eling studies of polyrhythmic networking motifs for multifunction central pattern generators comprised of the interneurons.

Here, we have demonstrated several computational techniques, developed by the author, which had been employed to give a thorough examination of the leech heart interneuron model. We would like to point out that all the methods are not model-specific and hence can be applied for a broad class of slow-fast neuronal models that are capable of tonic spiking and bursting generation. The methods include:

- The parameter continuation technique for localization of the slow-motion manifolds, quiescent and tonic spiking, in the phase space of the model without a need of the conventional slow-fast dissection. This method becomes of a particularly applicable value for the examination of such manifolds in models with several timescales; for example, such as the 14D canonical leech interneuron model [41], various elliptic bursters [51] including the original 4D Hodgkin–Huxley model, the 5–6D Terman–Rubin models for cells in basal ganglia, as well a 12D model of a sensory hair cell [74].
- The averaging approach has been enhanced for the detection of saddle-node bifurcations of periodic orbit in slow-fast models such as that of the leech heart interneuron.
- The apparatus of Poincaré return mappings for a voltage interval has been developed to study in detail all bifurcations, including nonlocal homoclinic,

Fig. 22 Three types of bistability in the leech heart interneuron: (A) bursting and depolarized quiescence, (B) tonic spiking and bursting and (C) tonic spiking and hyperpolarized quiescence. Switching between the activity pair is achieved by applying a negative or positive pulse to the targeted state



of tonic spiking and bursting, transitions between the oscillatory activity types, bistability and separating orbits, as well as various metric properties of the mappings such as the Lyapunov exponents, and topological entropy evaluated using the symbolic representation of the dynamics through the kneading invariants on this and other models, including the FitzHugh–Nagumo–Rinzel model for elliptic bursters [51].

- We have employed two, phenomenologically distinct, approaches to build the biparametric bifurcation diagrams of models [75]. While first numerical approach is “bifurcationally” native, the other, calculus-free approach, utilizes neuroscience plausible instruments for on-fly examination of temporal characteristics of the activity, which are extracted directly from voltage traces.
- We showed that the bistability is a robust, genuine phenomenon of this model, and that the dynamical states of the interneuron can be switched systematically by applying external pulses, hyper- or depolarizing.

Acknowledgements I would to thank Ph.D. students B. Chung, X. Hu, S. Jalil, and J. Wojcik for their assistance and multiple suggestions, and P. Channell, A. Neiman and R. Barrio for many stimulating discussions. The voltage mappings are due to P. Channell. This work has been supported by NSF Grant DMS-1009591, RFFI Grant No. 08-01-00083, the GSU Brains & Behavior Program, and “Grant opportunities for Russian scientists living abroad” project #14.740.11.0919.

References

1. Steriade, M., McCormick, D.A., Sejnowski, T.J.: Thalamocortical oscillations in the sleeping and aroused brain. *Science* **262**(5134), 679–685 (1993)
2. Terman, D., Rubin, J.E., Yew, A.C., Wilson, C.J.: Activity patterns in a model for the subthalamopallidal network of the basal ganglia. *J. Neurosci.* **22**(7), 2963–2976 (2002)
3. Bazhenov, M., Timofeev, I., Steriade, M., Sejnowski, T.: Spiking-bursting activity in the thalamic reticular nucleus initiates sequences of spindle oscillations in thalamic networks. *J. Neurophysiol.* **84**(2), 1076–1087 (2000)
4. Bazhenov, M., Timofeev, I., Fröhlich, F., Sejnowski, T.J.: Cellular and network mechanisms of electrographic seizures. *Drug Discov. Today Dis. Models* **5**(1), 45–57 (2008)
5. Cymbalyuk, G.S., Gaudry, Q., Masino, M.A., Calabrese, R.L.: Bursting in leech heart interneurons: Cell-

- autonomous and network-based mechanisms. *J. Neurosci.* **22**(24), 10580–10592 (2002)
6. Bertram, R., Butte, M.J., Kiemel, T., Sherman, A.: Topological and phenomenological classification of bursting oscillations. *Bull. Math. Biol.* **57**(3), 413–439 (1995)
 7. Canavier, C.C., Baxter, D.A., Clark, J.W., Byrne, J.H.: Nonlinear dynamics in a model neuron provide a novel mechanism for transient synaptic inputs to produce long-term alterations of postsynaptic activity. *J. Neurophysiol.* **69**(6), 2252–2257 (1993)
 8. Butera, R.J.: Multirhythmic bursting. *Chaos* **8**(1), 274–284 (1998)
 9. Frohlich, F., Bazhenov, M.: Coexistence of tonic firing and bursting in cortical neurons. *Phys. Rev. E, Stat. Nonlinear Soft Matter Phys.* **74**(3 Pt 1), 031922 (2006)
 10. Hounsgaard, J., Kiehn, O.: Serotonin-induced bistability of turtle motoneurons caused by a nifedipine-sensitive calcium plateau potential. *J. Physiol.* **414**, 265 (1898)
 11. Lechner, H., Baxter, F., Clark, C., Byrne, J.: Bistability and its regulation by Serotonin in the endogenously bursting neuron r15 in aplysia. *J. Neurophysiol.* **75**, 957 (1996)
 12. Turrigiano, G., Marder, E., Abbott, L.: Cellular short-term memory from a slow potassium conductance. *J. Neurophysiol.* **75**, 963–966 (1996)
 13. Kopell, N.: Toward a theory of modelling central pattern generators. In: Cohen, A.H., Rossingol, S., Grillner, S. (eds.) *Neural Control of Rhythmic Movements in Vertebrates*. Wiley, New York (1988)
 14. Marder, E., Calabrese, R.L.: Principles of rhythmic motor pattern generation. *Physiol. Rev.* **76**(3), 687–717 (1996)
 15. Briggman, K.L., Kristan, W.B.: Multifunctional pattern-generating circuits. *Annu. Rev. Neurosci.* **31**, 271–294 (2008)
 16. Kristan, W.B.: Neuronal decision-making circuits. *Curr. Biol.* **18**(19), R928–R932 (2008)
 17. Shilnikov, A.L., Gordon, R., Belykh, I.: Polyhythmic synchronization in bursting networking motifs. *Chaos* **18**(3), 037120 (2008)
 18. Wojcik, J., Clewley, R., Shilnikov, A.L.: Order parameter for bursting polyrhythms in multifunctional central pattern generators. *Phys. Rev. E, Stat. Nonlinear Soft Matter Phys.* (2011, in press)
 19. Rabinovich, M.I., Varona, P., Silverston, A.L., Abarbanel, H.D.: Dynamics principles in neuroscience. *Rev. Mod. Phys.* **78**(4), 1213–1265 (2006)
 20. Rinzel, J.: Bursting oscillations in an excitable membrane model. In: *Lecture Notes in Mathematics*, vol. 1151, pp. 304–316 (1985)
 21. Rinzel, J., Wang, X.J.: Oscillatory and bursting properties of neurons. In: Arbib, M. (ed.) *The Handbook of Brain Theory and Neural Networks*, pp. 686–691. MIT Press, Cambridge (1995)
 22. Rinzel, J., Ermentrout, B.: Analysis of neural excitability and oscillations. In: Koch, C., Segev, I. (eds.) *Computational Neuroscience*, pp. 135–169. MIT Press, Cambridge (1998)
 23. Guckenheimer, J.: Towards a global theory of singularly perturbed systems. *Prog. Nonlinear Differ. Equ. Appl.* **19**, 214–225 (1996)
 24. Izhikevich, E.M.: Neural excitability, spiking and bursting. *Int. J. Bifurc. Chaos* **10**, 1171–1266 (2000)
 25. Izhikevich, E.M.: *Dynamical Systems in Neuroscience. The Geometry of Excitability and Bursting*. MIT Press, Cambridge (2007)
 26. Tikhonov, A.N.: On the dependence of solutions of differential equations from a small parameter. *Mat. Sb.* **22**(64), 193–204 (1948)
 27. Pontryagin, L.S., Rodygin, L.V.: Periodic solution of a system of ordinary differential equations with a small parameter in the terms containing derivatives. *Sov. Math. Dokl.* **1**, 611–619 (1960)
 28. Fenichel, F.: Geometric singular perturbation theory for ordinary differential equations. *J. Differ. Equ.* **31**, 53–98 (1979)
 29. Mischenko, E.F., Rozov, N.K.: *Differential Equations with Small Parameters and Relaxation Oscillations*. Plenum, New York (1980)
 30. Mischenko, E.F., Kolesov, Yu.S., Kolesov, A.Yu., Rozov, N.Kh.: *Asymptotic Methods in Singularly Perturbed Systems*. Monographs in Contemporary Mathematics. Consultants Bureau, New York (1994)
 31. Jones, C.K.R.T., Kopell, N.: Tracking invariant-manifolds with differential forms in singularly perturbed systems. *J. Differ. Equ.* **108**(1), 64–88 (1994)
 32. Arnold, V.I., Afraimovich, V.S., Ilyashenko, Yu.S., Shilnikov, L.P.: *Dynamical Systems. Vol. V: Bifurcation Theory*. Encyclopaedia of Mathematical Sciences. Springer, Berlin (1994)
 33. Terman, D.: The transition from bursting to continuous spiking in excitable membrane models. *J. Nonlinear Sci.* **2**(2), 135–182 (1992)
 34. Holden, A.V., Fan, Y.S.: From simple to simple bursting oscillatory behaviour via intermittent chaos in the Rose–Hindmarsh model for neuronal activity. *Chaos Solitons Fractals* **2**, 349–369 (1992)
 35. Wang, X.J.: Genesis of bursting oscillations in the Hindmarsh–Rose model and homoclinicity to a chaotic saddle. *Physica D* **62**(1–4), 263–274 (1993)
 36. Feudel, U., Neiman, A., Pei, X., Wojtenek, W., Braun, H., Huber, M., Moss, F.: Homoclinic bifurcation in a Hodgkin–Huxley model of thermally sensitive neurons. *Chaos* **10**(1), 231–239 (2000)
 37. Deng, B., Hines, G.: Food chain chaos due to Shilnikov’s orbit. *Chaos* **12**(3), 533–538 (2002)
 38. Shilnikov, A.L., Rulkov, N.F.: Subthreshold oscillations in a map-based neuron model. *Phys. Lett. A* **328**(2–3), 177–184 (2004)
 39. Shilnikov, A.L., Calabrese, R.L., Cymbalyuk, G.: Mechanism of bistability: Tonic spiking and bursting in a neuron model. *Phys. Rev. E* **71**, 056214 (2005)
 40. Cymbalyuk, G., Shilnikov, A.L.: Coexistence of tonic spiking oscillations in a leech neuron model. *J. Comput. Neurosci.* **18**(3), 255–263 (2005)
 41. Channell, P., Cymbalyuk, G., Shilnikov, A.L.: Applications of the Poincare mapping technique to analysis of neuronal dynamics. *Neurocomputing* **70**, 10–12 (2007)
 42. Shilnikov, L.P., Shilnikov, A.L., Turaev, D., Chua, L.O.: *Methods of Qualitative Theory in Nonlinear Dynamics*, vol. 1. World Scientific, Singapore (1998)
 43. Shilnikov, L.P., Shilnikov, A.L., Turaev, D., Chua, L.O.: *Methods of Qualitative Theory in Nonlinear Dynamics*, vol. 2. World Scientific, Singapore (2001)

44. Shilnikov, A.L., Shilnikov, L.P., Turaev, D.V.: Blue sky catastrophe in singularly perturbed systems. *Mosc. Math. J.* **5**(1), 205–211 (2005)
45. Chay, T.R.: Chaos in a three-variable model of an excitable cell. *Physica D* **16**(2), 233–242 (1985)
46. Shilnikov, A.L., Rulkov, N.F.: Origin of chaos in a two-dimensional map modelling spiking-bursting neural activity. *Int. J. Bifurc. Chaos* **13**(11), 3325–3340 (2003)
47. Medvedev, G.M.: Reduction of a model of an excitable cell to a one-dimensional map. *Physica D* **202**(1–2), 87–106 (2005)
48. Griffiths, R.E., Pernarowski, M.C.: Return map characterizations for a model of bursting with two slow variables. *SIAM J. Appl. Math.* **66**(6), 1917–1948 (2006)
49. Channell, P., Fuwape, I., Neiman, A.B., Shilnikov, A.L.: Variability of bursting patterns in a neuron model in the presence of noise. *J. Comput. Neurosci.* **27**(3), 527–542 (2009)
50. Channell, P., Cymbalyuk, G., Shilnikov, A.: Origin of bursting through homoclinic spike adding in a neuron model. *Phys. Rev. Lett.* **98**(13), 134101 (2007)
51. Wojcik, J., Shilnikov, A.L.: Voltage interval mappings for dynamics transitions in elliptic bursters. *Physica D* (2011, accepted)
52. Shilnikov, A.L.: On bifurcations of the Lorenz attractor in the Shimizu–Morioka model. *Physica D* **62**(1–4), 338–346 (1993)
53. Belykh, V.N., Belykh, I.V., Colding-Jorgensen, M., Mosekilde, E.: Homoclinic bifurcations leading to bursting oscillations in cell models. *Eur. Phys. J. E, Soft Matter* **3**(3), 205–219 (2000)
54. Shilnikov, A.L., Cymbalyuk, G.: Homoclinic saddle-node orbit bifurcations en route between tonic spiking and bursting in neuron models, invited review. *Regul. Chaotic Dyn.* **3**(9), 281–297 (2004)
55. Doiron, B., Laing, C., Longtin, A., Maler, L.: Ghostbursting: A novel neuronal burst mechanism. *J. Comput. Neurosci.* **12**(1), 5–25 (2002)
56. Laing, C.R., Doiron, B., Longtin, A., Noonan, L., Turner, R.W., Maler, L.: Type I burst excitability. *J. Comput. Neurosci.* **14**(3), 329–342 (2003)
57. Rowat, P.F., Elson, R.C.: State-dependent effects of Na channel noise on neuronal burst generation. *J. Comput. Neurosci.* **16**(2), 87–112 (2004)
58. Shilnikov, A.L., Cymbalyuk, G.: Transition between tonic spiking and bursting in a neuron model via the blue-sky catastrophe. *Phys. Rev. Lett.* **94**(4), 048101 (2005)
59. Shilnikov, A.L., Kolomiets, M.L.: Methods of the qualitative theory for the Hindmarsh–Rose model: A case study. A tutorial. *Int. J. Bifurc. Chaos* **18**(7), 1–32 (2008)
60. Kramer, M.A., Traub, R.D., Kopell, N.J.: New dynamics in cerebellar Purkinje cells: Torus canards. *Phys. Rev. Lett.* **101**(6), 068103 (2008)
61. Gavrilov, N., Shilnikov, A.L.: *Methods of Qualitative Theory of Differential Equations and Related Topics.* AMS Transl. Series II (2000). Chapter Example of a blue sky catastrophe, pp. 99–105
62. Lukyanov, V., Shilnikov, L.P.: On some bifurcations of dynamical systems with homoclinic structures. *Sov. Math. Dokl.* **19**(6), 1314–1318 (1978)
63. Gavrilov, N.K., Shilnikov, L.P.: On three-dimensional dynamical systems close to systems with a structurally unstable homoclinic curve. *Math. USSR Sb.* **17**(3), 467–485 (1972)
64. Cymbalyuk, G.S., Calabrese, R.L.: A model of slow plateau-like oscillations based upon the fast Na⁺ current in a window mode. *Neurocomputing* **38**, 159–166 (2001)
65. Hodgkin, A.L., Huxley, A.F.: A quantitative description of membrane current and its application to conduction and excitation in nerve. *J. Physiol.* **117**(4), 500–544 (1952)
66. Sharkovsky, A.N., Kolyada, S.F., Sivak, A.G., Fedorenko, V.V.: *Dynamics of One-Dimensional Maps.* Mathematics and its Applications, vol. 407. Kluwer Academic, Dordrecht (1997)
67. Mira, C.: *Chaotic Dynamics from the One-Dimensional Endomorphism to the Two-Dimensional Diffeomorphism.* World Scientific, Singapore (1987)
68. Glendinning, P., Hall, T.: Zeros of the kneading invariant and topological entropy for Lorenz maps. *Nonlinearity* **9**, 999–1014 (1996)
69. Li, M.-C., Malkin, M.: Smooth symmetric and Lorenz models for unimodal maps. *Int. J. Bifurc. Chaos* **13**(11), 3353–3371 (2003)
70. Medvedev, G.M.: Transition to bursting via deterministic chaos. *Phys. Rev. Lett.* **97**, 048102 (2006)
71. Li, T.Y., Yorke, J.A.: Period three implies chaos. *Am. Math. Mon.* **82**(10), 985–992 (1975)
72. Shilnikov, L.P., Turaev, D.V.: Blue sky catastrophes. *Dokl. Math.* **51**, 404–407 (1995)
73. Barrio, R., Shilnikov, A.L.: Bursting dynamics of isolated and networked neurons (2011, in preparation)
74. Neiman, A., Shilnikov, A.L.: Spontaneous voltage oscillations and response dynamics of a Hodgkin–Huxley type model of sensory hair cells. *Phys. Rev. E, Stat. Nonlinear Soft Matter Phys.* (2011, submitted)
75. Barrio, R., Shilnikov, A.L.: Parameter-sweeping techniques for temporal dynamics of neuronal systems: Hindmarsh–Rose model. *J. Math. Neurosci.* (2011, in review)